

Two-Dimensional Bimetallic Hydroxide Nanostructures for Catalyzing Low-Temperature Aerobic C–H Bond Activation in Alkylarene and Alcohol Partial Oxidation

Abel Tetteh Sika-Nartey,[†] Yesim Sahin,[†] Kerem Emre Ercan, Zeynep Kap, Yusuf Kocak, Ayşe Dilay Erdali, Beyzanur Erdivan, Yunus Emre Türkmen,^{*} and Emrah Ozensoy^{*}



Cite This: *ACS Appl. Nano Mater.* 2022, 5, 18855–18870



Read Online

ACCESS |



Metrics & More



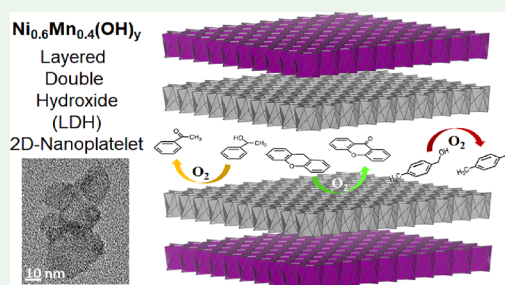
Article Recommendations



Supporting Information

ABSTRACT: Two-dimensional (2D) bimetallic $\text{Ni}_x\text{Mn}_{1-x}(\text{OH})_y$ layered double hydroxide (LDH) nanostructures were synthesized and optimized as a remarkably active catalytic platform for low-temperature aerobic C–H bond activation in alkylarenes and partial oxidation of alcohols using a wide substrate (*i.e.*, reactant) and diverse solvent scope. The $\text{Ni}_x\text{Mn}_{1-x}(\text{OH})_y$ structure consists of nonprecious and earth-abundant metals that can effectively operate at low catalyst loadings, requiring only molecular oxygen as the stoichiometric oxidant. Structurally diverse alkylarenes as well as primary and secondary alcohols were shown to be competent substrates where oxidation products were obtained in excellent yields (93–99%). Comprehensive catalyst structural characterization via XRD, ATR-IR, TEM, EDX, XPS, BET, and TGA indicated that the ultimately optimized $\text{Ni}_{0.6}\text{Mn}_{0.4}(\text{OH})_{y-9\text{S}}$ catalyst possessed not only particular rotational faults in its $\beta\text{-Ni}_{0.6}\text{Mn}_{0.4}(\text{OH})_y$ domains but also distinct $\alpha/\beta\text{-Ni}_{0.6}\text{Mn}_{0.4}(\text{OH})_y$ interstratification disorders, in addition to a relatively high specific surface area of $125\text{ m}^2/\text{g}$, a 2D platelet morphology, and an average Mn oxidation state of +3.5, suggesting the presence of both Mn^{3+} and Mn^{4+} species in its structure working in a synergistic fashion with the $\text{Ni}^{2+/x+}$ cations (the latter is justified by the lack of catalytic activity in the monometallic LDH catalysts $\text{Ni}(\text{OH})_2$ and $\text{Mn}(\text{OH})_2$). Kinetic isotope effect studies carried out in the fluorene oxidation reaction ($k_{\text{H}}/k_{\text{D}} = 5.7$) revealed that the rate-determining step of the catalytic oxidation reaction directly involved the scission of a C–H bond. Moreover, the optimized catalyst was demonstrated to be reusable through the application of a regeneration protocol, which can redeem the full initial activity of the carbon-poisoned spent catalyst in the fluorene oxidation reaction.

KEYWORDS: alcohol oxidation, C–H oxidation, layered double hydroxide, heterogeneous catalysis, alkylarene C–H activation



1. INTRODUCTION

Organic synthesis has traditionally been established on functional group interconversions where a pre-existing functional group is transformed into another using catalytic or noncatalytic methods. However, since the mid-1990s, the field has witnessed the entrance of the functionalization of unactivated C–H bonds to the organic synthesis toolbox with remarkable advances in catalytic C–H activation reactions.^{1–7} These advances not only extended our synthetic capabilities but also changed drastically our approach to retrosynthetic analysis.⁸ For instance, recent developments in the area of late-stage functionalization had a huge impact on medicinal chemistry and drug discovery.^{9–11} One important branch of such C–H activation reactions is the catalytic C–H oxidation reactions. In this reaction type, synthetically useful oxygenated products such as alcohols, ketones, aldehydes, or carboxylic acids can be accessed via catalytic oxidation of C–H bonds.^{12–19} On the other hand, catalysis of C–H bond oxidation reactions by heterogeneous catalytic systems is rather limited and underdeveloped compared to their homogeneous

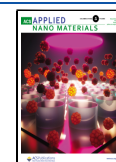
counterparts in terms of reactivity and selectivity.^{20,21} In this respect, development of reusable heterogeneous oxidation catalysts composed of nonprecious metals that operate under mild reaction conditions, with low catalyst loading, and with the use of molecular oxygen as the terminal oxidant is highly desired.²²

In heterogeneous catalysis, metal on metal oxide systems (*e.g.*, $\text{Pt}/\text{Al}_2\text{O}_3$),²³ metal oxide on metal oxide or activated carbon-based support materials (*e.g.*, VO_x/TiO_2 , $\text{PdO}_x/\text{carbon nanotubes}$),^{24,25} or metal-incorporated zeolite systems (*e.g.*, Rh-ZSM-5)²⁶ are among the ubiquitous architectures used in catalytic oxidation reactions. Although many of these catalysts are efficient in high-temperature reactions, they often suffer

Received: October 24, 2022

Accepted: November 21, 2022

Published: December 8, 2022



from low-temperature catalytic activity,^{27,28} which is crucial for decreasing process costs and enhancing sustainability. For instance, in the case of aerobic catalytic oxidation of alcohols, relatively few heterogeneous catalytic systems have been reported to have significant low-temperature activity such as Ru/Al₂O₃,²⁹ Au/TiO₂,³⁰ Pd/charcoal,³¹ CaLaScRuO_{6+δ},³² and RuO₂-FAU (faujasite zeolite),³³ most of which were composed of platinum group metals (PGMs), leading to high catalyst costs. As a part of our ongoing efforts toward the development of effective heterogeneous catalysts for alcohol and C–H bond oxidation reactions that work under aerobic conditions, we recently reported the utilization of LaMnO₃ as a perovskite-based catalyst for alkylarene oxidation and oxidative dimerization of 2-naphthol.³⁴ It should be noted that several other perovskite- and metal-oxide-based materials have been shown to be effective catalysts for C–H oxidation reactions.^{35–38}

In our quest to develop heterogeneous oxidation catalysts with higher activity and selectivity, we next turned our focus to nonprecious metal hydroxide-containing catalytic systems, which can be exploited in low-temperature catalytic processes as promising alternatives to the existing conventional PGM-based oxidation catalysts.³⁹ PGM-free metal hydroxide nano-material architectures constitute a versatile catalytic platform because they can be synthetically fine-tuned to exhibit unique 2D structures, morphology, and electronic and magnetic properties that can be optimized for a wide range of different low-temperature reactions.³⁹ Moreover, metal hydroxides and mixed metal hydroxides have been utilized in a variety of advanced applications such as battery technologies, electro-synthesis, supercapacitors, electrochromic devices, and electro-chemical sensors.⁴⁰ In this respect, whereas Ni(OH)_x has recently been successfully employed as a catalyst or cocatalyst in various transformations including hydrogen production,^{41,42} water oxidation,⁴³ and benzylic C–H borylation reactions,⁴⁴ the utilization of nickel-based mixed metal hydroxide systems in heterogeneous catalysis has been extremely limited.

Along these lines, in the current work, we demonstrate that PGM-free 2D mixed metal hydroxide systems with optimized nanostructures can serve as exceptionally active and selective catalysts in low-temperature C–H activation reactions involving the partial oxidation of a variety of alkylarenes and alcohols that can surpass PGM-containing conventional catalysts. Strikingly, these structurally versatile PGM-free layered double hydroxide (LDH) catalysts can also outperform the conventional PGM-containing catalysts in the literature without the need for any additives, promoters, or performance boosters. Our detailed catalyst characterization studies indicate that 2D mixed metal LDH systems offer a variety of tunable structural parameters such as (i) crystallographic phases of the LDH domains, (ii) types and extents of stacking faults between the LDH layers, (iii) intercalation of different crystallographic domains, (iv) interlayer water content, (v) interlayer spacing, (vi) relative cation ratio (*i.e.*, Ni/Mn), (vii) oxidation state of the transition metal centers, and (viii) specific surface area (SSA), which can be readily altered to modify the catalytic functionality of these systems for different catalytic applications.

2. EXPERIMENTAL SECTION

2.1. Catalyst Optimization Parameters. During the catalyst synthesis and optimization studies, the influence of five different factors on the catalyst structure and/or performance was investigated:

(a) metal hydroxide synthesis method (*i.e.*, solvothermal vs chemical precipitation methods), (b) nominal metal cation ratio (*i.e.*, Ni/Mn), (c) NaOH concentration used in the chemical precipitation method, (d) extent of the residual Na⁺ and Cl[−] ions present on the catalyst surface, and (e) type of the solvent used in the catalytic performance tests.

2.1.1. Catalyst Synthesis for the Comparison between Solvothermal vs Chemical Precipitation Methods. NiCl₂·6H₂O (≥98% purity, Merck), MnCl₂·2H₂O (≥99% purity, Merck), and NaOH (≥98% purity, Merck) were used in the catalyst synthesis as received. The nominal stoichiometric concentration of NaOH(aq) required for the synthesis of the currently investigated mixed metal hydroxides (*i.e.*, Ni_xMn_{1−x}(OH)₂) assuming the presence of divalent metal cations was 2.06 M. Hereafter, this stoichiometric concentration will be denoted as “S”, and the catalysts will be named as Ni_xMn_{1−x}(OH)₂-*n*S, where *n*S indicates the NaOH(aq) concentration used in the catalyst synthesis. For the comparison of the two different metal hydroxide synthesis methods (*i.e.*, solvothermal vs chemical precipitation methods), the Ni_{0.5}Mn_{0.5}(OH)₂-3S catalyst was chosen because a NaOH(aq) concentration of 3S is expected to provide sufficient hydroxylation for this bimetallic composition. This Ni/Mn cation ratio of 1:1 (by mol) was selected because Ni_{0.5}Mn_{0.5}(OH)₂-3S showed 99% conversion of 9*H*-xanthene (xanthene, **1a**) to 9*H*-xanthen-9-one (xanthone, **1b**), corresponding to more than three times higher catalytic activity compared to that of Ni(OH)₂-3S and Mn(OH)₂-3S (24 and 28%, respectively) with the use of the same catalyst amount of 100 mg. It must be noted that these three catalysts used in this pilot test were synthesized by the solvothermal method at 403 K.

In both of the utilized synthetic methods (*i.e.*, solvothermal or chemical precipitation), calculated amounts of NiCl₂·6H₂O and MnCl₂·2H₂O (Table S1) were dissolved in 20 mL of deionized water. In addition, the calculated amount of NaOH(s) was dissolved separately in 20 mL of deionized water. These two solutions were stirred at 600 and 400 rpm, respectively, for a period of 30 min. Prior to mixing, the stirring speed of the NaOH(aq) solution was increased to 1500 rpm. Then, Ni–Mn solution was added to the NaOH(aq) solution. The resulting mixture was stirred at 1500 rpm for 1 min followed by stirring at a lower speed of 600 rpm for 1 h. Then, the mixture was immediately transferred into a Teflon line. The Teflon line was then inserted into an autoclave and heated in a drying oven either at 403 K for 12 h or at 343 K for 72 h. Next, the sample was removed from the autoclave and washed six times with deionized water. After that, the sample was divided into four identical portions and centrifuged at a rate of 6000 rpm for 3 min. This was followed by drying the obtained suspensions in a 400 mL beaker at 333 K for 24 h. Note that in the chemical precipitation method, the autoclave-heating step was omitted, whereas the remaining aforementioned steps were carried out as described above.

2.1.2. Nominal Metal Cation Ratio Optimization in the Chemical Precipitation Method. Initial catalytic performance tests on the aerobic oxidation of 9*H*-xanthene (xanthene, **1a**) to 9*H*-xanthen-9-one (xanthone, **1b**) showed that the chemical precipitation synthesis method outperformed the solvothermal synthesis method. Thus, to find the optimized nickel–manganese hydroxide catalyst to be synthesized by the chemical precipitation method, the nominal Ni/Mn ratio was varied while keeping the NaOH(aq) concentration constant at 6S (see Table S1 for the exact precursor amounts). This 6S NaOH concentration was chosen for the nominal metal cation ratio optimization because in a pilot test, we discovered that the Ni_{0.7}Mn_{0.3}(OH)₂-6S catalyst outperformed Ni_{0.7}Mn_{0.3}(OH)₂-3S (both of which were synthesized by the chemical precipitation method) in the aerobic oxidation of xanthene (**1a**) to xanthone (**1b**) (*i.e.*, using the same catalyst amount (5 mg), Ni_{0.7}Mn_{0.3}(OH)₂-6S and Ni_{0.7}Mn_{0.3}(OH)₂-3S resulted in 67 and 28% conversion, respectively). Also, the NaOH(aq) concentration of 6S was employed at this stage to ensure the complete hydroxylation of the catalysts with different Ni or Mn cation valencies.

2.1.3. NaOH Concentration Optimization in the Chemical Precipitation Method. Experiments on the optimization of metal

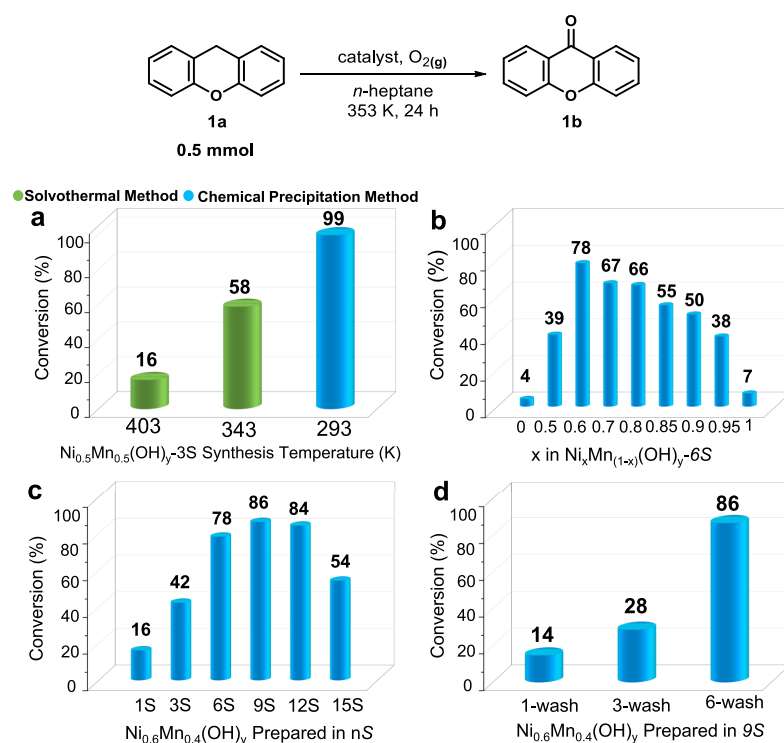


Figure 1. Aerobic oxidation of xanthene (**1a**) to xanthone (**1b**). Catalytic activity data for (a) 10 mg of Ni_{0.5}Mn_{0.5}(OH)_y-3S catalysts prepared via the solvothermal method at 343 or 403 K and the chemical precipitation method at 293 K (catalysts were washed six times after the synthesis); (b) 5 mg of Ni_xMn_(1-x)(OH)_y-6S catalysts synthesized with different nominal Ni/Mn cation ratios via the chemical precipitation method at 293 K (catalysts were washed six times after the synthesis); (c) 5 mg of Ni_{0.6}Mn_{0.4}(OH)_y catalysts prepared with different NaOH(aq) concentrations via the chemical precipitation method at 293 K (catalysts were washed six times after the synthesis); and (d) 5 mg of Ni_{0.6}Mn_{0.4}(OH)_y-9S catalysts synthesized with the chemical precipitation method at 293 K washed once, thrice, or six times in the aerobic oxidation of xanthene (**1a**) to xanthone (**1b**) under the conditions described in the uppermost section of the figure. S stands for a NaOH(aq) concentration of 2.06 M.

cation stoichiometric ratio revealed that Ni_{0.6}Mn_{0.4}(OH)_y exhibited the best performance in the aerobic oxidation of xanthene (**1a**) to xanthone (**1b**). Using this particular metal cation stoichiometric ratio, the concentration of NaOH(aq) was systematically varied to further optimize the catalyst structure and performance. Accordingly, preparation of the Ni_{0.6}Mn_{0.4}(OH)_y catalyst was carried out using NaOH(aq) concentrations of 1S, 3S, 6S, 9S, 12S, and 15S. Note that 15S is a concentration value that is close to the saturation concentration of NaOH(aq) in pure water at 293 K (*i.e.*, 1.26 g of NaOH in 1 mL of H₂O at 293 K).⁴⁵

2.2. Catalytic Performance Tests. Liquid-phase catalytic activity tests were carried out in a custom-design catalytic reactor described in Figure S1. In a typical catalytic performance test, proper amounts of catalysts, which are specified in the further sections, and 2.0 mL of *n*-heptane (solvent) were loaded into an oven-dried 25 mL Schlenk flask. Next, the flask was filled with 1 bar of O₂ (g) and sealed with a stopcock. In the control experiments carried out under anaerobic conditions, the solvent was deoxygenated via the freeze–pump–thaw technique, and N₂(g) was used as the inert atmosphere medium. The reaction mixture was stirred at 400 rpm in an oil bath at various temperatures and for different durations as described in detail in the forthcoming sections. At the end of a typical catalytic performance test reaction, the mixture was cooled to room temperature, diluted with ethyl acetate (EtOAc) or dichloromethane (DCM), and passed through Celite. Conversion values for the catalytic oxidation reactions were determined by ¹H NMR spectroscopic analysis. Flash column chromatography was utilized as the purification method with the use of Silicycle 40–63 μm (230–400 mesh) flash silica gel as the stationary phase.

2.3. Catalyst Characterization. A Bruker Alpha Platinum Fourier transform infrared (FTIR) spectrometer equipped with an attenuated total reflectance (ATR) diamond crystal module and a

deuterated triglycine sulfate (DTGS) mid-IR detector was used to acquire ATR-IR spectra. ATR-IR data were registered with a resolution of 2 cm⁻¹ and 128 scans per spectrum. X-ray diffraction (XRD) experiments were carried out with a PANalytical (X'Pert PRO) Multi-Purpose X-Ray diffractometer equipped with a Cu Kα (1.5405 Å) X-Ray source operated at 45 kV/40 mA. During the XRD experiments, powder catalyst samples were analyzed within a 2θ range of 10–80° using a scan step size of 0.01° and a time per step of 35 s. Brunauer, Emmett, and Teller (BET) specific surface area (SSA) measurements were executed with a Micromeritics Tristar 3000 surface area and pore size analyzer via a five-point method. An FEI Technai G2F30 transmission electron microscope (TEM) was used to carry out TEM and energy dispersive X-ray (EDX) measurements. During the TEM sample preparation, powdered catalysts were dispersed in ethanol by sonication followed by drop casting the mixture on a lacey carbon-coated copper grid. TEM imaging was performed under bright-field conditions. A Thermo Scientific K-Alpha X-ray photoelectron spectrometer (ESCALAB 250) was utilized to acquire the XPS spectra. Monochromatic Al Kα radiation (1486.6 eV) was exploited to stimulate photoemission. A pass energy of 200 eV was chosen for the XPS survey spectra (3 scans/spectrum), whereas high-resolution XPS spectra were acquired with a 30 eV pass energy (200 scans/spectrum for Mn3s and 50 scans/spectrum for other elements). A C1s binding energy (B.E.) of 284.8 eV corresponding to the adventitious carbon species was utilized in the calibration of the B.E. values. XPS data analysis was carried out via the CasaXPS software, and background subtraction was performed by using a Shirley background. Thermal gravimetric analysis (TGA) experiments were executed with a TA Instruments TGA Q500 instrument where 8.5 mg of the catalyst was heated under 60 mL/min N₂(g) flow from 303 to 1223 K with a linear temperature ramp of 10 K/min. ¹H NMR spectra at 400 MHz and ¹³C NMR spectra at 100 MHz were recorded

with a Bruker DPX 400 NMR spectrometer. Calibration of the NMR data was carried out with an internal standard (tetramethylsilane, TMS, 0 ppm) or residual solvent signal (chloroform; 7.26 ppm for ^1H NMR spectra and 77.16 ppm for ^{13}C NMR spectra).

3. RESULTS AND DISCUSSION

3.1. Catalytic Performance Tests for the Oxidation of Xanthene to Xanthone. Results of the catalytic performance tests for the aerobic oxidation of xanthene (**1a**) to xanthone (**1b**) on monometallic and bimetallic hydroxide catalysts prepared by varying four different synthesis parameters are presented in Figure 1.

3.1.1. Influence of the Catalyst Synthesis Method. Figure 1a compares the influence of the catalyst preparation method in the aerobic oxidation of 0.5 mmol of xanthene (**1a**) that was carried out using 10 mg of the $\text{Ni}_{0.5}\text{Mn}_{0.5}(\text{OH})_y\text{-3S}$ catalyst prepared with two different synthesis methods. As can be seen in Figure 1a, the catalyst prepared via the chemical precipitation method at 293 K yields the oxidation product xanthone (**1b**) with almost full conversion (99%) and significantly outperforms the catalysts synthesized with the solvothermal method at 343 or 403 K. The solvothermal method is typically carried out at temperatures less than 473 K.⁴⁰ Thus, two different temperatures (343 and 403 K) were chosen to examine the effect of the solvothermal synthesis temperature on the xanthene (**1a**) oxidation (Figure 1a). Solvothermal synthesis at a lower temperature of 343 K yielded not only a higher xanthene (**1a**) conversion (Figure 1a) but also a smaller average catalyst particle size of ca. 8 nm estimated via XRD analysis using the Scherrer equation (data not shown) as compared to the solvothermal synthesis at 403 K leading to a lower xanthene (**1a**) conversion and a larger average catalyst particle size of ca. 16 nm. Along these lines, we utilized an even lower synthesis temperature of 293 K for the chemical precipitation method that resulted in higher xanthene (**1a**) conversion (Figure 1a) and smaller average catalyst particle size (ca. 2 nm) than the solvothermal synthesis method. Thus, in the rest of the catalyst optimization studies, chemical precipitation at 293 K was chosen as the primary method of synthesis.

3.1.2. Effect of the Nominal Ni/Mn Metal Cation Ratio. Next, the effect of the Ni/Mn nominal metal cation ratio on the catalytic performance was investigated via the use of 5 mg of catalyst per 0.5 mmol of substrate, where the catalyst synthesis was carried out with a $\text{NaOH}(\text{aq})$ concentration of 6S. Figure 1b clearly demonstrates that monometallic hydroxides (*i.e.*, $\text{Mn}(\text{OH})_y\text{-6S}$ and $\text{Ni}(\text{OH})_y\text{-6S}$) exhibit the lowest catalytic activities for xanthene (**1a**) oxidation with conversion values of 4 and 7%, respectively. Interestingly, in the case of $\text{Ni}_{0.95}\text{Mn}_{0.05}(\text{OH})_y\text{-6S}$ involving the incorporation of only 5% Mn to the monometallic $\text{Ni}(\text{OH})_y$ structure, a drastic (ca. 5-fold) boost in catalytic activity was observed, yielding a xanthene (**1a**) conversion of 38%. This important observation points to a synergistic interaction between Ni and Mn sites in the bimetallic $\text{Ni}_x\text{Mn}_{1-x}(\text{OH})_y\text{-6S}$ hydroxide system, suggesting that the catalytic properties of these nanomaterials can be fine-tuned by controlling the relative compositions of different metal cations. Figure 1b also exhibits a typical volcano-type plot revealing the optimum relative metal cation stoichiometric ratio, where the maximum catalytic activity for aerobic xanthene (**1a**) oxidation is observed for $\text{Ni}_{0.6}\text{Mn}_{0.4}(\text{OH})_y\text{-6S}$. Indeed, the oxidation product xanthone

(**1b**) was observed to form with 78% conversion via the use of only 5 mg of the $\text{Ni}_{0.6}\text{Mn}_{0.4}(\text{OH})_y\text{-6S}$ catalyst.

3.1.3. Impact of the $\text{NaOH}(\text{aq})$ Concentration. After the identification of the optimal Ni/Mn nominal cation ratio in the catalyst structure, we proceeded with the investigation of the effect of $\text{NaOH}(\text{aq})$ concentration used in the catalyst preparation on the catalytic activity. As can be seen in Figure 1c, extremely low or extremely high $\text{NaOH}(\text{aq})$ concentrations lead to limited catalytic activities (16, 42, and 54% conversion values for 1S, 3S, and 15S of $\text{NaOH}(\text{aq})$ concentrations, respectively), whereas the catalytic performance was observed to reach a maximum value (86% conversion) for the $\text{Ni}_{0.6}\text{Mn}_{0.4}(\text{OH})_y\text{-9S}$ catalyst.

3.1.4. Influence of Residual Na^+ and Cl^- Species on the Catalyst Surface. We also investigated the effect of the presence of residual Na^+ and Cl^- ions originating from the basic medium used in the synthesis and the metal precursors, respectively, on the catalytic aerobic oxidation of xanthene (**1a**) (Figure 1d). To this end, the optimized catalyst (*i.e.*, $\text{Ni}_{0.6}\text{Mn}_{0.4}(\text{OH})_y\text{-9S}$) was washed with one, three, or six subsequent cycles of deionized water before the final drying stage. Surface elemental composition analysis carried out by XPS for these samples given in Table S2 suggested that although the catalyst surface revealed significant amounts of Na (23%) and Cl (1%) after a single wash, washing three times with deionized water led to a decrease in the Na content to 3%, whereas Cl content did not change significantly. On the other hand, applying six consecutive washing cycles resulted in the almost complete removal of Na^+ and Cl^- species from the catalyst surface, and their concentrations fell below the analytical detection limit of XPS. Furthermore, Table S2 indicates that increasing the number of washing cycles also monotonically increases the detected surface concentrations of Ni and Mn species on the catalyst surface as well as the corresponding catalytic conversion values (Figure 1d) as a result of the removal of surface Na^+ and Cl^- species and uncovering of the catalytically active transition metal sites. It is interesting to note that although the surface elemental compositions of the catalysts after three and six washing cycles are rather similar in terms of their relative Ni and Mn surface concentrations, their catalytic conversion values differ by ca. 300%, respectively. This stark variation in catalytic activity can be ascribed to the presence of minute amounts of Na^+ and Cl^- species on the catalyst surface in the former case acting as strong catalytic inhibitors.

3.1.5. Effect of the Solvent Type Used in the Catalytic Aerobic Xanthene Oxidation Tests. The catalyst optimization studies summarized in Figure 1 led to the identification of the $\text{Ni}_{0.6}\text{Mn}_{0.4}(\text{OH})_y\text{-9S}$ bimetallic hydroxide that is washed with deionized water for six successive cycles as the optimal catalyst for the oxidation of xanthene (**1a**) to xanthone (**1b**) in *n*-heptane. Thus, a brief solvent screening study was also employed in an attempt to investigate the compatibility of the $\text{Ni}_{0.6}\text{Mn}_{0.4}(\text{OH})_y\text{-9S}$ catalyst to xanthene (**1a**) oxidation in different solvents. As discussed earlier, utilization of 5 mg of the $\text{Ni}_{0.6}\text{Mn}_{0.4}(\text{OH})_y\text{-9S}$ catalyst with 0.5 mmol of xanthene (**1a**) in *n*-heptane yielded a xanthone (**1b**) conversion of 86% (Figure 1c). To amplify the variation of the catalytic performance as a function of solvent type, in the solvent scope experiments, we used 7 mg of $\text{Ni}_{0.6}\text{Mn}_{0.4}(\text{OH})_y\text{-9S}$ (Table S3), which yielded full conversion (>99%) in *n*-heptane. It should be noted that, in this experiment, oxidation product **1b** was isolated in 96% yield after purification by

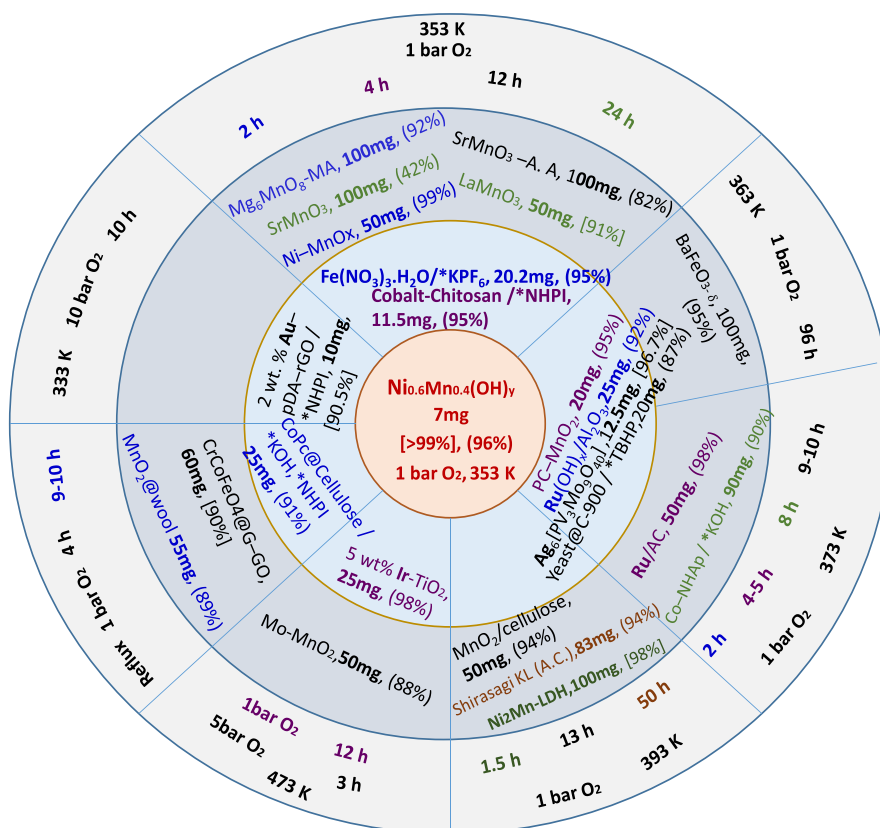


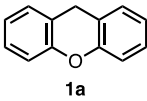
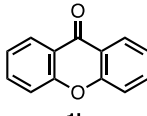
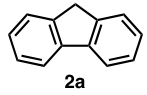
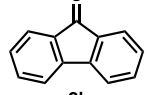
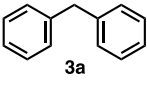
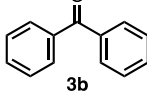
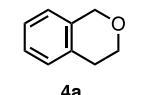
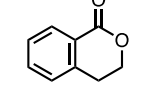
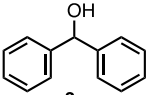
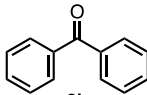
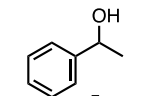
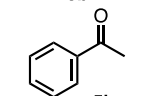
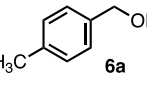
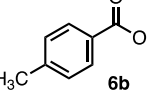
Figure 2. Graphical compilation of the literature data given in Table S4 for the comparison of the catalytic activity performances of various heterogeneous catalytic systems in the literature and the currently synthesized $\text{Ni}_{0.6}\text{Mn}_{0.4}(\text{OH})_y$ -9S catalyst in the aerobic oxidation of xanthone to xanthone. Note that the catalyst amounts were normalized to 0.5 mmol of the substrate (*i.e.*, xanthone). Chemicals with (*) correspond to external additives included in the reaction mixture to boost the catalytic performance. Conversion values are given in square brackets, and isolated yields are presented in parentheses. NHPI: *N*-hydroxyphthalimide. Corresponding references, reaction conditions, and further details are provided in Table S4.

column chromatography. In addition to *n*-heptane, we also examined toluene and benzotrifluoride (α,α,α -trifluorotoluene)⁴⁶ as aromatic nonpolar and polar solvents, respectively. Pleasingly, both of these latter solvents were found to be compatible media for the catalytic oxidation reaction, providing xanthone product **1b** with high conversion values (93 and 92%, respectively; Table S3). In other words, these solvents do not influence the reaction mechanism at the solid-liquid interface by neither competing for active sites with the reactants nor co-catalyzing the reaction.⁴⁷ However, considering the solvent Kamlet-Taft dipolarity/polarizability values (π^*)^{48,49} of the three solvents (Table S3), it can be argued that whereas *n*-heptane is not expected to reveal significant solvating effects on the reactive species, toluene and benzotrifluoride may exhibit significant solvating effects by influencing the reaction mechanism⁴⁷ and xanthone conversions (Table S3). Although current results indicate that all these three solvents can be used effectively, *n*-heptane was typically selected as the reaction medium for most of the remaining studies reported in the current work owing to the highest catalytic performance observed in this solvent. As a slightly longer straight chain alkane, *n*-octane was also used as a solvent in some of the currently investigated reactions requiring higher temperatures. Note that for substrates having low solubility in *n*-heptane or *n*-octane, benzotrifluoride can be considered as a suitable alternative medium due to its more polar nature.

3.1.6. Comparison of the Catalytic Performance of Bimetallic Hydroxides with the Existing Catalysts in the Literature for Aerobic Xanthone Oxidation. Table S4 lists the detailed reaction parameters and performance results of the currently reported $\text{Ni}_{0.6}\text{Mn}_{0.4}(\text{OH})_y$ -9S bimetallic hydroxide catalyst as well as other heterogeneous catalysts reported in the literature for the catalytic aerobic oxidation of xanthone (**1a**) to xanthone (**1b**). Figure 2 also illustrates a graphical compilation of the data given in Table S4, where the results were normalized to 0.5 mmol of xanthone (**1a**) (as the starting material) for easy comparison. Figure 2 clearly indicates that the $\text{Ni}_{0.6}\text{Mn}_{0.4}(\text{OH})_y$ -9S catalyst developed in the current work outperforms all of the PGM-containing and PGM-free catalysts in the literature by affording xanthone (**1b**) with >99% conversion and 96% isolated product yield using the lowest catalyst amount (*i.e.*, 7 mg) at the lowest O_2 pressure (*i.e.*, 1 bar) and at one of the lowest reaction temperatures (*i.e.*, 353 K). Furthermore, unlike some of the high-performing catalysts given in Figure 2, which require inclusion of various additives, promoters, or performance boosters (labeled with "*" in Figure 2), the $\text{Ni}_{0.6}\text{Mn}_{0.4}(\text{OH})_y$ -9S catalyst does not require the use of any additives, rendering it economically and ergonomically the most preferable catalyst. In some other cases, high performance was obtained by refluxing of the solvent, which is also not required for $\text{Ni}_{0.6}\text{Mn}_{0.4}(\text{OH})_y$ -9S.

3.1.7. Time-Dependent Aerobic Xanthone Oxidation with $\text{Ni}_{0.6}\text{Mn}_{0.4}(\text{OH})_y$ -9S in *n*-Heptane. In the next stage of our

Table 1. Scope of the C–H Oxidation and Alcohol Oxidation Reactions Catalyzed by $\text{Ni}_{0.6}\text{Mn}_{0.4}(\text{OH})_y\text{-9S}^a$

Entry	Substrate	Catalyst amount (mg)	Product	Conversion/Isolated product yield (%)
1 ^b	 1a	7	 1b	>99 / 96
2 ^b	 2a	20	 2b	>99 / 99
3 ^c	 3a	20	 3b	92 / 94
4 ^c	 4a	20	 4b	96 / 96
5 ^b	 3c	10	 3b	>99 / 99
6 ^b	 5a	30	 5b	>99 / 93
7 ^c	 6a	30	 6b	>99 / 96

^aReaction conditions: 0.50 mmol of substrate, 1 bar O_2 , 24 h. ^b*n*-Heptane (2 mL) and 353 K, and ^c*n*-Octane (2 mL) and 383 K. Isolated product yields refer to yields obtained after purification by column chromatography.

studies, we examined the kinetic behavior of the xanthene oxidation catalyzed by $\text{Ni}_{0.6}\text{Mn}_{0.4}(\text{OH})_y\text{-9S}$ to investigate the time dependence of the conversion values. In separate identical reactor vessels, the catalytic mixture containing 7 mg of the $\text{Ni}_{0.6}\text{Mn}_{0.4}(\text{OH})_y\text{-9S}$ catalyst, xanthene (1a), and *n*-heptane was heated at 353 K, and conversion values were determined at 6, 12, 18, and 24 h. It was found out that the reaction proceeds in a very fast manner with more than 80% conversion in the first 6 h of the reaction, whereas it reaches almost full conversion (96%) at the end of 12 h (Figure S2).

3.2. Aerobic Oxidation of Other Alkylarenes and Alcohols Catalyzed by $\text{Ni}_{0.6}\text{Mn}_{0.4}(\text{OH})_y\text{-9S}$. To demonstrate that the remarkably high activity of the $\text{Ni}_{0.6}\text{Mn}_{0.4}(\text{OH})_y\text{-9S}$ catalyst developed in this work was not limited only to the oxidation of xanthene (1a), we tested its performance in the aerobic oxidation of other alkylarenes and alcohols. Initially, C–H oxidation of 9H-fluorene (2a) was achieved by using 20 mg of catalyst per 0.50 mmol of substrate at 353 K, and the oxidation product 9H-fluoren-9-one (fluorenone, 2b) was observed to form with >99% conversion (Table 1, entry 2). Isolation of the product by flash column chromatography gave pure product 2b in 99% yield, demonstrating an excellent agreement between isolated product yield and conversion

value determined by ^1H NMR spectroscopy. These results underscore the high catalytic performance of the optimized $\text{Ni}_{0.6}\text{Mn}_{0.4}(\text{OH})_y\text{-9S}$ catalyst compared to the activity of a recently reported NiMn LDH catalyst that requires 100 mg of catalyst per 0.5 mmol of substrate at a higher reaction temperature (*i.e.*, 393 K) in similar C–H oxidation reactions (Figure 2 and Table S4).⁵⁰ When a relatively less reactive substrate, diphenylmethane (3a), was used along with the same catalyst loading at a slightly higher temperature (383 K), the oxidation product benzophenone (3b) was obtained with 92% conversion and an isolated product yield of 94% (Table 1, entry 3). After the successful demonstration of the newly developed catalytic protocol for the oxidation of doubly benzylic C–H bonds, we next turned our attention to the oxidation of isochroman (4a), which possesses two different types of benzylic C–H bonds. As a result of the oxidation of isochroman derivatives, isochromanones can be obtained. These latter chemicals are significant scaffolds in a variety of natural products with important biological activities.⁵¹ Gratifyingly, the optimized conditions were also observed to be effective for the oxidation of isochroman (4a), and the formation of isochromanone (4b) was attained with high conversion (96%) and high yield (96%) by using a catalyst

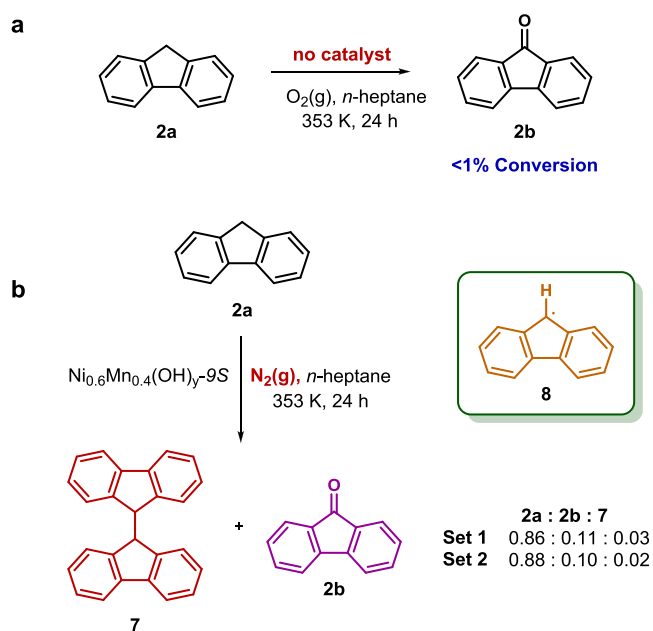
loading of 20 mg and 0.5 mmol of substrate at 383 K (Table 1, entry 4). This result also underscores that the newly developed catalytic method can be applied to the C–H oxidation of heterocyclic compounds as well. Additionally, the formation of compound **4b** with complete selectivity shows that this catalytic protocol can be employed for the synthesis of lactones by oxidative functionalization at the α -C–H bonds of cyclic ethers. Of particular note is the complete lack of catalytic activity of the previously reported NiMn LDH catalyst in the oxidation of isochroman (**4a**) even after 48 h.⁵⁰

With the successful demonstration of catalytic C–H oxidation reactions, we next investigated the effectiveness of the $\text{Ni}_{0.6}\text{Mn}_{0.4}(\text{OH})_y\text{-9S}$ catalyst on the oxidation of primary and secondary alcohols. When diphenylmethanol (**3c**) was tested as a benzylic alcohol substrate, oxidation product benzophenone (**3b**) was obtained with an excellent yield (99%) by using 10 mg of the catalyst at 353 K (Table 1, entry 5). The reaction of DL-*sec*-phenethyl alcohol (**5a**) with 30 mg of the catalyst at 353 K afforded acetophenone (**5b**) in excellent conversion (>99%) and high yield (93%; Table 1, entry 6). We next focused on the catalytic oxidation of a benzylic primary alcohol. For this purpose, 4-methylbenzyl alcohol (**6a**) was oxidized in the presence of 30 mg of the $\text{Ni}_{0.6}\text{Mn}_{0.4}(\text{OH})_y\text{-9S}$ catalyst and 1 bar $\text{O}_2(\text{g})$ at 383 K, and *p*-toluic acid (4-methylbenzoic acid, **6b**) was obtained with >99% conversion and 96% yield (Table 1, entry 7). It should be noted that oxidation of this substrate occurred selectively on the primary alcohol part rather than the benzylic – CH_3 group.

3.3. Mechanistic Studies. To shed light on the details of the mechanism of the $\text{Ni}_{0.6}\text{Mn}_{0.4}(\text{OH})_y\text{-9S}$ catalyzed oxidation reactions, several control experiments were performed. First, the oxidation of fluorene (**2a**) was tested under the same reaction conditions but in the absence of any catalysts to justify that the presence of the catalyst is crucial for the activation of molecular oxygen and/or the reactant. In agreement with our expectations, the conversion of fluorene (**2a**) to fluorenone (**2b**) under these conditions was less than <1%, demonstrating the requisite role of the catalyst for the oxidation reaction (Scheme 1a). In a second set of control experiments, the oxidation of fluorene (**2a**, 0.50 mmol) was run under an inert atmosphere of $\text{N}_2(\text{g})$ using 20 mg of the $\text{Ni}_{0.6}\text{Mn}_{0.4}(\text{OH})_y\text{-9S}$ catalyst at 353 K for 24 h. The solvent was deoxygenated by the freeze–pump–thaw technique to minimize the amount of molecular oxygen in the reaction medium. This experiment was run in duplicate and resulted in an average of 11% conversion to the ketone product **2b** and 3% conversion to the dimerization product **7**, whereas 87% of the reactant fluorene (**2a**) remained intact, demonstrating the significance of molecular oxygen for the oxidation process (Scheme 1b). The small amount of ketone formation may be due to the incomplete deoxygenation of the solvent or the penetration of adventitious oxygen to the reaction mixture.

Observation of the formation of the dimerization product **7** is important and reveals valuable insights on the reaction mechanism. This is because the dimerization product **7** can only be obtained by the homocoupling of the radical intermediate **8** in which this radical is formed by a hydrogen atom abstraction from the starting material at the beginning of the reaction. Then, intermediate **8** may react with the activated molecular oxygen to form the corresponding oxidation product, whereas in the absence of oxygen, it has to react with itself to construct 9*H*,9'*H*-9,9'-bifluorene (**7**). It should also be emphasized that the formation of the dimer **7** was not

Scheme 1. Effect of (a) the $\text{Ni}_{0.6}\text{Mn}_{0.4}(\text{OH})_y\text{-9S}$ Catalyst and (b) Oxygen on the Reaction Outcome

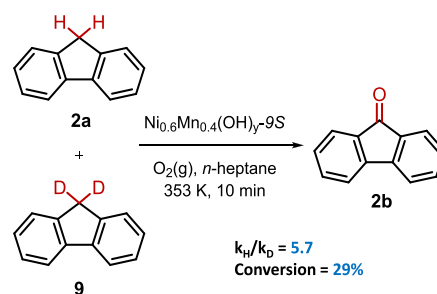


seen in any of the previous experiments involving molecular oxygen as the sole oxidant, in agreement with one of our recent studies where we utilized LaMnO_3 (i.e., perovskite-type) catalysts for the aerobic oxidation reactions.³⁴

Note that additional control experiments were also carried out in the absence of a catalyst by using xanthene (**1a**), fluorene (**2a**), and diphenylmethane (**3a**) as substrates and NaOH or KOH as Brønsted basic catalysts (Table S5). As expected, these control experiments lacking any bimetallic hydroxide catalysts also did not reveal any significant extent of products.

3.4. Elucidating the Rate-Determining Step in Fluorene Oxidation via Kinetic Isotope Effect Experiments. In an attempt to gain insight on the rate-determining step of the catalytic C–H oxidation reaction, kinetic isotope effect experiments were carried out.⁵² First, commercial fluorene (**2a**) was isotopically labeled with deuterium at the 9-position by treatment with NaH in $\text{DMSO-}d_6$ followed by quenching with D_2O .⁵³ Following this protocol, fluorene- d_2 (**9**) was obtained with 98% deuterium incorporation and in 92% yield after purification. Then, a 1:1 mixture of fluorene (**2a**) and fluorene- d_2 (**9**) was subjected to the optimized reaction conditions as a set of two runs using 20 mg of the $\text{Ni}_{0.6}\text{Mn}_{0.4}(\text{OH})_y\text{-9S}$ catalyst (Scheme 2). This provided an

Scheme 2. Kinetic Isotope Effect Experiments in Aerobic Fluorene Oxidation



environment in which C–H and C–D bond functionalization occurred under identical conditions to give more reliable results. The reactions were quenched after 10 min at ca. 30% conversion to stay in the kinetic region. The % consumption values of fluorene (**2a**) and fluorene-*d*₂ (**9**) were determined by a careful ¹H NMR spectroscopic analysis. The average value of the ratio of the nondeuterated to deuterated reaction rate constants (*i.e.*, k_H/k_D) was found to be 5.7, which was clearly indicative of the presence of a primary kinetic isotope effect (1° KIE) in the reaction.⁵⁴ Therefore, it can be interpreted that the rate-determining step or the product-determining step of the catalytic oxidation reaction directly involved the scission of a C–H bond. The average ¹H NMR yield for fluorenone (**2b**) was determined as 33% when 1,3,5-trimethoxybenzene was used as an internal standard under these conditions.

3.5. Structural Characterization of the Bimetallic Hydroxide Catalysts. Two different polymorphs (*i.e.*, α - and β -layered double hydroxide, LDH crystallographic phases) of Ni(OH)₂ have been reported in the literature (Figure 3a,b).⁴⁰ ATR-IR spectroscopic investigation of the –OH

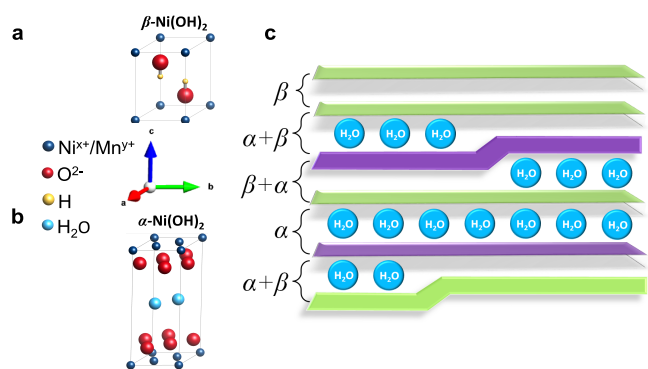


Figure 3. Crystal structures of (a) pure β -Ni(OH)₂ and (b) pure α -Ni(OH)₂ layered double hydroxide (LDH) phases and (c) illustration of the possible variations in the interlayer spacings and α/β -interstratification in the Ni_xMn_y(OH)_{y-n}S catalysts containing both α - and β -LDH phases.⁴⁰

vibrational features observed within 3000–4000 cm⁻¹ can be useful to distinguish between these different Ni(OH)₂ polymorphs. This is mostly due to the fact that the α -Ni(OH)₂ phase reveals an LDH structure (Figure 3b), where water molecules are incorporated in between the adjacent nickel hydroxide layers that are separated by a wide distance (note that the separation between the Ni²⁺ cation layers in the α -Ni(OH)₂ lattice structure is ca. 8.0 Å)⁴⁰ and can undergo H-bonding that results in a broad and a convoluted vibrational spectroscopic signature within 3000–3600 cm⁻¹.⁵⁵ In the α -Ni(OH)₂ structure, water molecules between the layers are not located at fixed sites and may rotate and/or translate in the *ab*-crystallographic plane. Thus, the α -Ni(OH)₂ structure is known to reveal a turbostratic nature, where relative orientations of the layers are random along the *ab*-crystallographic plane.⁴⁰

In contrast, the β -Ni(OH)₂ phase (Figure 3a) lacks any interlayer water molecules in its lattice system and possesses an LDH structure with a narrower separation of 4.6 Å⁴⁰ between the Ni²⁺ cation layers, revealing isolated hydroxide sites that cannot engage in H-bonding. As a result, the β -Ni(OH)₂ phase exhibits sharp and blue-shifted vibrational spectroscopic features located within 3200–3600 cm⁻¹.⁵⁵ Obviously, Ni-

(OH)₂ structures containing both α - and β -phases (Figure 3c) yield a combination of these aforementioned –OH vibrational spectroscopic signatures.

Figure 4a,b presents the ATR-IR spectra corresponding to the Ni_xMn_{1-x}(OH)_y-6S catalysts given in Figure 1b that were used in the optimization of the nominal Ni/Mn cation ratio in the catalyst formulation. It can be inferred from Figure 4a that Ni_xMn_{1-x}(OH)_y-6S catalysts with $x \leq 0.7$ predominantly exhibit a bimetallic α -LDH phase. On the other hand, a higher Ni content, *i.e.*, $0.8 \leq x \leq 0.95$, leads to the presence of both bimetallic α - and β -LDH phases, whereas the monometallic Ni(OH)₂-6S catalyst synthesized in the current work mostly reveals the monometallic β -LDH phase. Vibrational features observed in Figure 4 are consistent with the characteristic vibrational signatures of metal hydroxides. Namely, the lowest frequency peaks at 437 and 473 cm⁻¹ in Figure 4b can be attributed to typical “A_{1g} + acoustic mode” combination signals, whereas the next set of slightly higher frequency features present in Figure 4b,d at 504, 525, and 596 cm⁻¹ can be assigned to E_g + A_{2u} (TO) or E_g + E_u (TO) combination modes.⁵⁵ Bands at 947 and 1067 cm⁻¹ are ascribed to E_u (LO) O–H bending modes, and the vibrational signatures at 1358 and 1450 cm⁻¹ are due to E_g + A_{2u} (TO) combination bands.⁵⁵ The weak feature at 836 cm⁻¹ is tentatively assigned to MnO(OH) minority species.⁵⁶ Finally, the peak at 1630 cm⁻¹ is associated with adsorbed water molecules on the surface of the metal hydroxide catalysts.⁵⁵ In addition, current XRD analysis suggests that in the absence of Ni, Mn₃O₄ phases are also formed. Thus, in the absence of Ni (Figure 4a,b), contribution from Mn₃O₄ phases to the ATR-IR spectra is also likely.

Figure 4c,d depicts the ATR-IR spectra for Ni_{0.6}Mn_{0.4}(OH)_y-*n*S catalysts prepared via the chemical precipitation method using various NaOH(aq) concentrations that were used in the catalyst optimization series given in Figure 1c. It can be inferred from Figure 4c that Ni_{0.6}Mn_{0.4}(OH)_y synthesized with NaOH(aq) concentrations of 1S, 3S, and 6S predominantly exhibit a bimetallic α -LDH phase. On the other hand, higher concentrations of NaOH(aq) lead to the presence of both bimetallic α - and β -LDH phases.

ATR-IR data shown in Figure 4 are quite informative as they clearly indicate that by carefully controlling the nominal Ni/Mn cation ratio and the NaOH(aq) concentration used in the synthesis, one can readily fine-tune the (a) relative extents of α - and β -LDH phases, (b) interlayer separations in the LDH structure, (c) presence/absence of interlayer water molecules, and (d) nature of the hydrogen bonding interactions in the interlayer region. These important structural factors may have a direct impact on the coordination/oxidation state of the transition metal active sites; adsorption/desorption strengths of reactants, intermediates, and products; as well as their corresponding kinetics associated with adsorption, desorption, and transport. This critical structural versatility can presumably be an efficient strategy to customize 2-D mixed metal double hydroxide systems to target particular reactants in a variety of other catalytic reactions. In this respect, we propose that intercalation of the α -LDH layers with molecules possessing relatively flat geometries may play a role in the success of our newly developed catalytic oxidation method. Indeed, intercalation of L-proline as an organocatalyst⁵⁷ and titanium tartrate as a metal complex catalyst⁵⁸ in LDH hosts has been utilized successfully by others as a catalyst immobilization strategy.³⁹ Moreover, 9-methylanthracene, another flat mole-

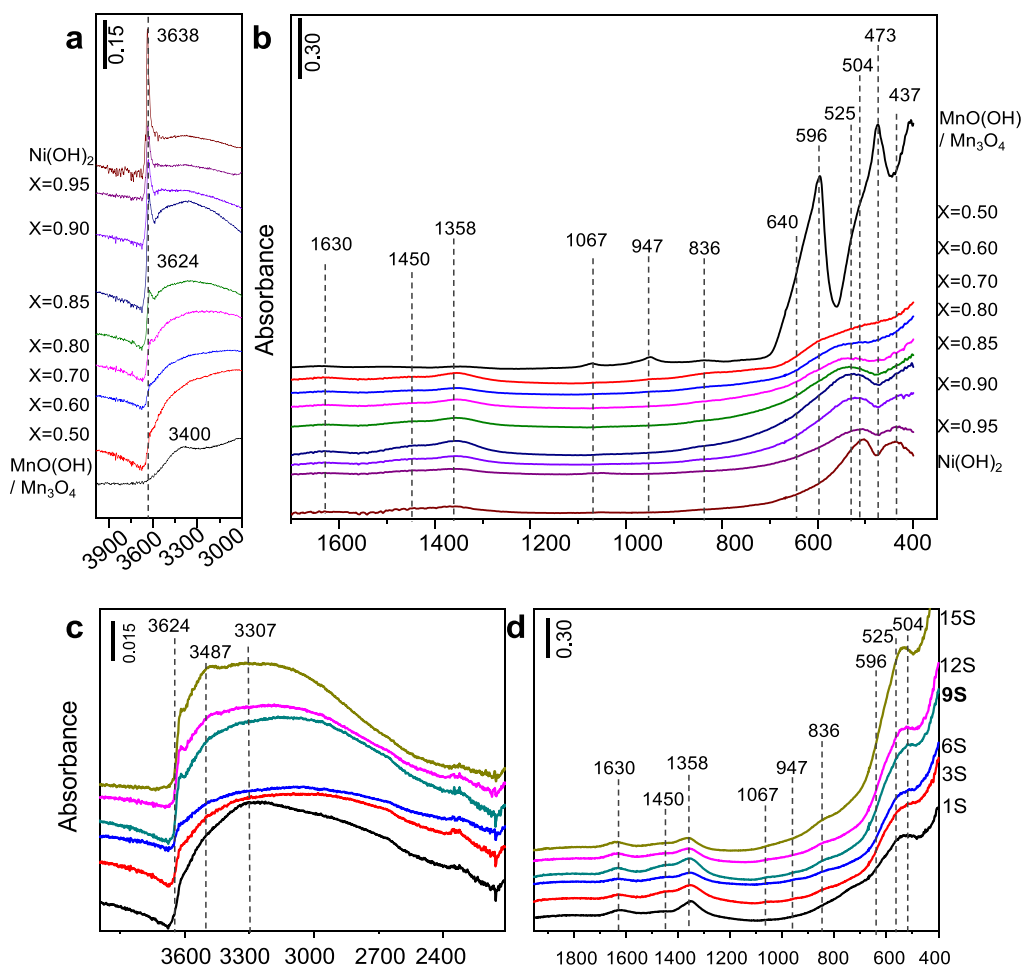


Figure 4. ATR-IR spectra for (a, b) $\text{Ni}_x\text{Mn}_{1-x}(\text{OH})_y\text{-6S}$ catalysts ($0 \leq x \leq 1$) and (c, d) $\text{Ni}_{0.6}\text{Mn}_{0.4}(\text{OH})_y$ catalysts prepared with $\text{NaOH}(\text{aq})$ concentrations of nS ($1 \leq n \leq 15$). Catalysts were washed six times after the synthesis.

cule with an aromatic backbone, was shown by single-crystal X-ray crystallography to be incorporated into a cleft formed by two aromatic groups of a supramolecular host with a separation of ca. 7 Å.⁵⁹ Therefore, an $\text{Ni}_{0.6}\text{Mn}_{0.4}(\text{OH})_y\text{-9S}$ interlayer distance of ca. 9 Å that can be estimated using the LDH XRD signal at $2\theta = 19.2^\circ$ observed in Figure 5 is expected to be geometrically suitable for the entrance of the aromatic reactants to the interlayer space. As can be seen in Table S6, the average pore diameter of the currently optimized $\text{Ni}_{0.6}\text{Mn}_{0.4}(\text{OH})_y\text{-9S}$ catalyst is ca. 50 Å, which is also sufficiently large to accommodate the relevant reactants. Thus, from a strictly geometric point of view, currently studied substrates may be accommodated on the external surface, in the pores, as well as the in the interlayer spacings of the LDH structure. Although we do not have a particular experimental method in our repertoire that can conclusively yield the precise location of the catalytic active sites, on the basis of the unique rotational faults in its $\beta\text{-Ni}_{0.6}\text{Mn}_{0.4}(\text{OH})_y$ domains and its distinct $\alpha/\beta\text{-Ni}_{0.6}\text{Mn}_{0.4}(\text{OH})_y$ interstratification disorders, it is likely that interlayer spacings could be contributing to the reactivity, in addition to the other conventional catalytic active sites existing on the external surface of the $\text{Ni}_{0.6}\text{Mn}_{0.4}(\text{OH})_y\text{-9S}$ nanoparticles. Accordingly, it is apparent that the ultimately optimized catalyst for the xanthene (1a) oxidation in the current work ($\text{Ni}_{0.6}\text{Mn}_{0.4}(\text{OH})_y\text{-9S}$) contains a unique combination of a predominantly bimetallic α -LDH phase

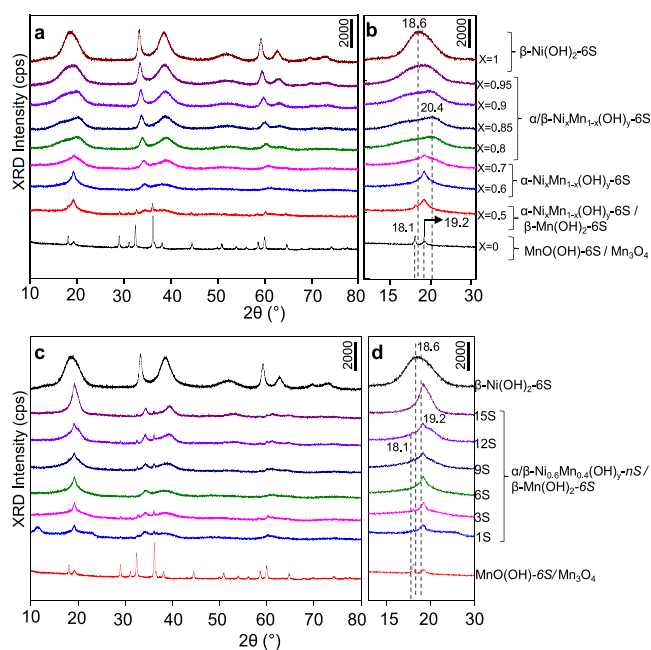


Figure 5. XRD data for (a, b) $\text{Ni}_x\text{Mn}_{1-x}(\text{OH})_y\text{-6S}$ ($0 \leq x \leq 1$) and (c, d) $\text{Ni}_{0.6}\text{Mn}_{0.4}(\text{OH})_y$ catalysts prepared in a $\text{NaOH}(\text{aq})$ concentration of nS ($1 \leq n \leq 15$). Catalysts were washed six times after the synthesis.

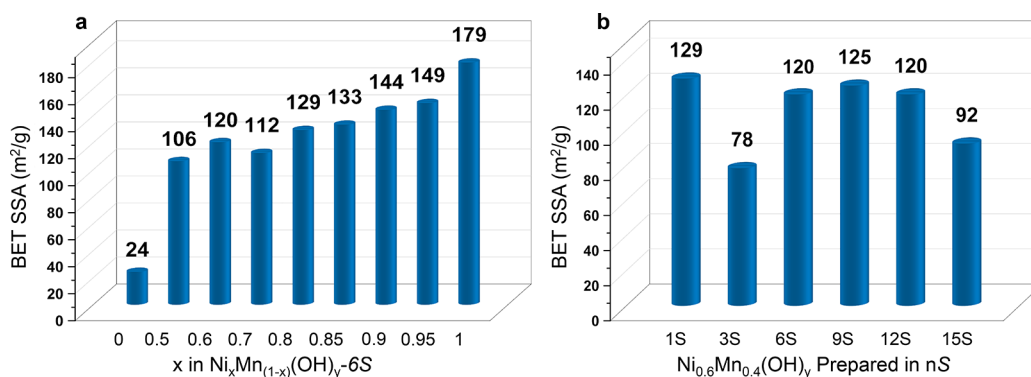


Figure 6. BET SSA values for (a) Ni_xMn_{1-x}(OH)_y-6S catalysts ($0 \leq x \leq 1$) and (b) Ni_{0.6}Mn_{0.4}(OH)_y-nS catalysts ($1 \leq n \leq 15$) prepared via the chemical precipitation method.

with a minor but detectable contribution from a bimetallic β -LDH phase.

Furthermore, catalytic inhibition/poisoning of the currently investigated bimetallic hydroxide catalysts can also be (at least in part) explained in light of their layered double hydroxide interlayer structure. For instance, poisoning of the Ni_{0.6}Mn_{0.4}(OH)_y-9S catalyst due to the presence of residual Na⁺ and Cl⁻ ions (Table S2) can be associated with the disruption of the interlayer spacings due to the ion exchange between the LDH cations/anions and Na⁺/Cl⁻ ions. For instance, substitution of OH⁻ ions having an ionic radius of 1.37 Å⁶⁰ with Cl⁻ ions possessing a larger ionic radius of 1.81 Å⁶⁰ is likely to cause structural alterations in the interlayer spacings and α/β -interstratification.

XRD data of the LDH systems can provide valuable insights on the different types of structural disorders existing in the crystal structure. Strong intralayer interactions between cations and anions within the LDH sheets along with the relatively weaker interlayer interactions between these layers result in well-known structural disorders.⁴⁰ Stacking fault disorders in the β -LDH phase such as rotations of the layers about the crystallographic *c* axis or translation of these layers within the *ab*-crystallographic plane (note that rotational/translational stacking faults are not relevant for α -LDH phases as these phases are already turbostratic in nature with randomly oriented layers) as well as α/β -interstratifications were reported to have different characteristic effects on the measured XRD signals of metal hydroxides.⁴⁰ Accordingly, rotational stacking faults between the β -LDH phase layers result in selective line broadening in XRD peaks without a peak shift, as they occur along the direction of the crystallographic *c* axis.⁴⁰ Broadening due to the stacking faults is typically observed for the (001), (101), and (111) XRD signals of β -Ni(OH)₂ located at ca. $2\theta = 19.3$, 38.6 , and 62.8° , respectively.⁴⁰ However, in the case of α/β -interstratifications, relevant XRD signals undergo both peak shifts and peak broadening.⁴⁰

Figure 5a,b shows the effect of the nominal Ni/Mn metal cation ratio on the crystal structure of the Ni_xMn_{1-x}(OH)_y-6S catalysts whose catalytic performance results are presented in Figure 1b. On the basis of the XRD data presented in Figure 5a,b, it can be stated that for $x = 1$, the Ni(OH)₂-6S catalyst exhibits a monometallic β -LDH phase (ICDD PDF Card No. 04-016-0358), whereas with the decreasing Ni loading in the bimetallic hydroxide structure (*i.e.*, for $0.8 \leq x \leq 0.95$), both bimetallic α -LDH⁴⁰ and bimetallic β -LDH phases start to appear. This is evident by the observation of peak shifts in the

XRD signals of Ni_xMn_{1-x}(OH)_y-6S for $0.8 \leq x \leq 0.95$ toward higher 2θ values (Figure 5b) as compared to those of β -Ni(OH)₂-6S, indicating the formation of α/β -interstratifications in Ni_xMn_{1-x}(OH)_y-6S ($0.8 \leq x \leq 0.95$). Furthermore, the additional broadening of the XRD signals and the decreasing XRD signal intensities for $0.8 < x \leq 1$ (Figure 5a,b) are also consistent with the increase in the extent of the turbostratic (and thus relatively disordered) bimetallic α -LDH phase present in the Ni_xMn_{1-x}(OH)_y-6S structure.⁴⁰

On the other hand, a further decrease in the Ni loading (*i.e.*, within $0.6 \leq x \leq 0.7$) results in the observation of a mostly bimetallic α -LDH phase with only minor contributions from a bimetallic β -LDH phase. It is worth mentioning that for $x = 0.5$ (Ni_{0.5}Mn_{0.5}(OH)_y-6S), in addition to α - and β -Ni_{0.5}Mn_{0.5}(OH)_y phases, the presence of a monometallic MnO(OH) phase (ICDD PDF Card No. 00-018-0804) is also likely. Finally, in the case where Ni is completely removed from the LDH structure, the catalyst denoted as Mn(OH)₂-6S ($x = 0$) reveals Mn₃O₄ (ICDD PDF Card No. 04-005-9818) and MnO(OH) phases. It should be noted that XRD data described above are also in good agreement with the current ATR-IR data (Figure 4a).

Figure 5c,d shows that Ni_{0.6}Mn_{0.4}(OH)_y synthesized with NaOH(aq) concentrations of 1S–15S exhibit a mostly bimetallic α/β -LDH phase (evident by the characteristically broad diffraction features with low intensities due to the disordered turbostratic structure of bimetallic α -LDH phase), as well as a minor contribution from monometallic β -Mn(OH)₂. On the other hand, in the case of 9S, 12S, and 15S, the sharpening and growth of the XRD signals suggest enhanced crystallographic ordering and a greater contribution from the bimetallic β -LDH phase in addition to bimetallic α -LDH and monometallic β -Mn(OH)₂ phases. Hence, it is apparent that the ultimately optimized Ni_{0.6}Mn_{0.4}(OH)_y-9S catalyst possesses a layered double hydroxide structure containing not only particular rotational faults in its β -Ni_{0.6}Mn_{0.4}(OH)_y domains but also distinct α/β -Ni_{0.6}Mn_{0.4}(OH)_y interstratification disorders in addition to a smaller contribution from β -Mn(OH)₂.

Figure 6a shows the BET SSA measurements for Ni_xMn_{1-x}(OH)_y-6S catalysts synthesized with various nominal Ni/Mn cation ratios whose catalytic performance results are presented in Figure 1b. Figure 6a suggests that Mn(OH)₂-6S possesses the lowest SSA value of 24 m²/g, whereas Ni(OH)₂-6S has the highest BET SSA value of 179 m²/g, suggesting that increasing the Ni content in the mixed metal hydroxide structure typically increases the SSA value. For a NaOH(aq)

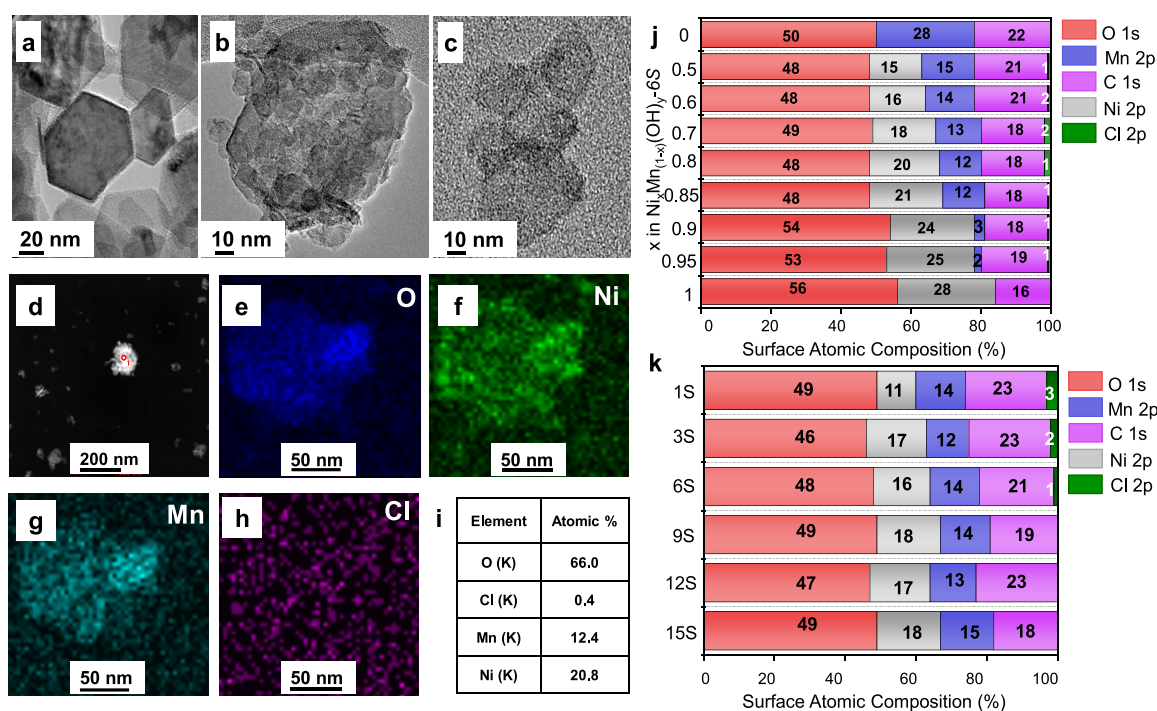


Figure 7. TEM images of (a) Ni(OH)₂-3S synthesized by the solvothermal method and (b, c) Ni_{0.6}Mn_{0.4}(OH)_y-9S catalysts prepared via the chemical precipitation method. (d) TEM image; (e–h) EDX elemental mapping for O, Ni, Mn, and Cl; and (i) EDX atomic percentages. XPS surface atomic composition values for (j) Ni_xMn_{1-x}(OH)_y-6S catalysts (0 ≤ x ≤ 1) and (k) Ni_{0.6}Mn_{0.4}(OH)_y-nS catalysts (1 ≤ n ≤ 15). Catalysts were washed six times during synthesis.

concentration of 6S, the catalyst showing the highest xanthene (1a) oxidation activity (Figure 1b) is Ni_{0.6}Mn_{0.4}(OH)_y, which exhibits an SSA of 120 m²/g (Figure 6a). Data given in Figure 6a point to the fact that SSA is not the foremost structural property governing the ultimate catalytic reactivity because the catalyst with the highest SSA of 179 m²/g (*i.e.*, Ni(OH)₂-6S) has a lower activity than that of Ni_{0.6}Mn_{0.4}(OH)_y-6S.

Figure 6b presents the BET SSA values for the catalyst optimization series given in Figure 1c. As can be seen in Figure 6b, Ni_{0.6}Mn_{0.4}(OH)_y-1S has the highest SSA value (129 m²/g), which is consistent with the extremely broad XRD peaks observed for this catalyst (Figure 5d) indicating poor structural order and a large number of structural imperfections/defects. It is apparent that a NaOH(aq) concentration of 1S is not sufficient for the establishment of sufficiently organized bimetallic α - or β -LDH phases, limiting the corresponding catalytic reactivity despite a very high SSA. It can be realized that for higher NaOH(aq) concentrations than 1S, Ni_{0.6}Mn_{0.4}(OH)_y catalysts show a volcano-type plot, where the SSA maximizes at 9S. Thus, it can be argued that for NaOH(aq) concentration >1S, bimetallic α/β -LDH domains can be constructed in an effective manner, and increasing the base concentration up to 9S leads to the efficient hydroxylation of the metal hydroxide layers and possibly exfoliation of the 2D metal hydroxide layers resulting in increasing SSA. For excessive NaOH(aq) concentrations greater than 9S, the strongly basic medium starts to influence the catalyst structure in a detrimental manner by altering the different phases/domains as shown in the current XRD (Figure 5c,d) and ATR-IR (Figure 4c,d) results. In addition, excessive hydroxylation of the catalyst surface at NaOH(aq) concentrations >9S can also lead to the poisoning of the active metal cations on the surface by blocking these sites via –OH adsorption.

Figure 7a shows the highly ordered two-dimensional (2D) nanoplatelets of Ni(OH)₂-3S prepared via the solvothermal method exhibiting a well-defined hexagonal structure. TEM images of the optimized Ni_{0.6}Mn_{0.4}(OH)_y-9S catalyst illustrated in Figure 7b,c reveal a unique morphology where a layered and 2D structure is also visible. On the other hand, 2D-Ni_{0.6}Mn_{0.4}(OH)_y-9S nanoparticles show a poorly defined and rather disordered hexagonal/polyhedral geometry with diameters typically ranging between ca. 5 and 80 nm. Structural information deduced from TEM images (Figure 7b,c) is also consistent with the corresponding XRD data (Figure 5c,d) suggesting the presence of an LDH crystal structure possessing multiple crystallographic phases with various types of structural defects.

TEM/EDX analysis of the optimized Ni_{0.6}Mn_{0.4}(OH)_y-9S catalyst (Figure 7d–i) verifies the presence of both Ni and Mn in the catalyst composition, where the atomic concentration ratio of Ni/Mn was found to be 20.8:12.4, which corresponds to a stoichiometry of Ni_{0.63}Mn_{0.37}(OH)_y, in excellent agreement with the nominal metal precursor loading used in the synthesis (*i.e.*, Ni_{0.6}Mn_{0.4}(OH)_y). EDX data also clearly indicate that the chloride ions of the metal precursors are almost entirely eliminated from the catalyst structure, whereas Ni and Mn species are distributed rather uniformly on the 2D nanoplatelets.

Detailed surface atomic compositions of the synthesized mixed metal hydroxide samples were also investigated via XPS (Figure 7j,k). Figure 7j presents the surface atomic compositions for the catalyst optimization series given in Figure 1b and reveals that with the increasing nominal Ni precursor concentration used in the synthesis, surface concentrations of Ni and O atoms monotonically increase whereas Mn surface concentration typically decreases.

Furthermore, Figure 7k shows that varying NaOH(aq) concentrations used in the synthesis does not yield a clear trend in the surface atomic composition of the elements present on the catalysts. However, NaOH(aq) concentrations of 1S, 3S, and 6S are apparently not sufficient to remove all of the chloride ions originating from the metal precursors, and the complete chloride removal is observed for NaOH(aq) concentrations $\geq 9S$.

Comprehensive XPS measurements were carried out to investigate the electronic structural changes for the catalysts used in the catalytic performance optimization series given in Figure 1b,c, and these XPS data are presented in Figure S3a–c and d–f, respectively. The complex nature of the Ni2p XPS spectra of oxidized and hydroxylated Ni systems has been discussed in detail in the literature by Biesinger et al.⁶¹ In this former report, it was reported that because of the (a) spin–orbit splitting, (b) asymmetric nature of the Ni2p_{3/2} and Ni2p_{1/2} features, (c) presence of additional satellite and multiplet splitting features, (d) need for complex Shirley background offsets, and (e) possible existence of a large number of different Ni species (e.g., Ni, NiO, α/β -Ni(OH)₂, γ/β -NiOOH, etc.), making precise assignments regarding the chemical environment of Ni species can be often challenging. Thus, rather than attempting a full spectroscopic analysis, in the current work, we will only provide tentative assignments regarding the Ni 2p XPS data. Figure S3a shows that general aspects of the Ni2p spectra belonging to the Ni_xMn_{1-x}(OH)_y-6S catalysts ($0 < x \leq 1$) agree with an LDH structure.⁶¹ Whereas the Ni2p_{3/2} feature of the Ni(OH)₂ (i.e., $x = 1$) catalyst at 855.0 eV can be predominantly attributed to a β -Ni(OH)₂ structure (which is also supported by the current ATR-IR and XRD results given in Figures 4 and 5, respectively), the presence of a minor amount of NiOOH along with an even smaller extent of NiO cannot be ruled out. As can be seen in Figure S3a, incorporation of Mn to the Ni(OH)₂ LDH structure results in ca. +0.3 eV shift in the Ni2p_{3/2} signal, which may presumably suggest either an increase in the relative extent of the LDH domains (i.e., a decrease in the extents of metal oxide and metal oxyhydroxide domains) or an increase in the oxidation state of Ni species. Figure S3a clearly illustrates that Mn incorporation leads to alterations in the chemical environment of Ni species and the associated electronic structure of the Ni sites.

Corresponding Mn2p XPS spectra of the Ni_xMn_{1-x}(OH)_y-6S ($0 \leq x < 1$) catalysts are presented in Figure S3b. Some of the aforementioned complications regarding the interpretation of the Ni2p XPS spectra discussed above are also partly valid for the Mn2p XPS spectra. In accordance with previous studies⁶² on Mn-doped Ni(OH)₂ nanostructures, Figure S3b depicts that small loadings of Mn (i.e., $x = 0.95$ – 0.90) result in an extremely broad and convoluted Mn2p envelope that may be attributed to the presence of Mn⁴⁺, Mn³⁺, and Mn²⁺ species.^{63–66} Increasing Mn loading within $0.5 \leq x \leq 0.85$ leads to a convoluted Mn2p feature centered at ca. 642.3 eV that can be attributed to the presence of mostly Mn⁴⁺ with a small extent of Mn³⁺ species and a much smaller contribution from Mn²⁺ species.^{63–66} Furthermore, in the absence of any Ni (i.e., for $x = 0$ or Mn(OH)₂), the Mn2p XPS spectrum reveals features that can be ascribed to mostly Mn³⁺ and Mn²⁺ species.^{63–66} This is also in agreement with the observation of Mn₃O₄ and MnO(OH) phases for this sample in the current ATR-IR and XRD measurements as shown in Figures 4 and 5. It is worth mentioning that the Mn3s XPS spectrum can also

provide further insight regarding the average oxidation state (AOS) of Mn sites.⁶⁷ It is well known that Mn3s signals have two distinct multiplet split components due to coupling of the nonionized 3s electron with 3d valence-band electrons resulting in peak splitting values (i.e., Δ) varying in correlation with the Mn oxidation state (e.g., $\Delta = 6.0, 5.3,$ and 4.7 eV for MnO/Mn²⁺, Mn₂O₃/Mn³⁺, and MnO₂/Mn⁴⁺, respectively). Accordingly, AOS of the Mn species can be estimated using the Mn3s splitting energies using the following equation: AOS = $8.95 - 1.13\Delta$.⁶⁷ Because of the weaker XPS cross section of the Mn3s features as compared to that of Mn2p features, utilizing Mn3s signals for the catalysts with relatively low Mn loadings is difficult. Thus, we estimated the Mn AOS values for the catalyst where we can detect Mn3s features with high analytical confidence such as Ni_{0.6}Mn_{0.4}(OH)_y-9S (Figure S4a,b). These results indicate that the AOS of Mn species for the Ni_{0.6}Mn_{0.4}(OH)_y-9S catalyst is +3.4, which is in very good agreement with the general interpretation of the corresponding Mn2p XPS signals suggesting the presence of mostly Mn⁴⁺ and Mn³⁺ species and a smaller contribution from Mn²⁺ species.

O1s XPS data for the Ni_xMn_{1-x}(OH)_y-6S ($0 \leq x \leq 1$) catalysts depicted in Figure S3c indicate that Ni(OH)₂ (i.e., for $x = 1$) reveals a broad and convoluted O1s peak centered at 530.2 that can be associated with predominantly β -Ni(OH)₂ and, to a lesser extent, NiOOH and NiO domains. Incorporation of Mn to the LDH structure ($0.85 \leq x \leq 0.95$) yields a O1s B.E. shift of +0.5 eV, which is consistent with the coexistence of bimetallic α/β -LDH phases with different –OH functionalities and dissimilar hydrogen bonding structure as suggested by the current ATR-IR and XRD results presented in Figures 4 and 5, respectively. Finally, for Mn(OH)₂ (i.e., $x = 0$) containing Mn₃O₄ and MnO(OH) phases, the O1s XPS spectrum displays two features composed of a major signal at 529.9 eV and a minor feature of 531.3 eV that can be associated with –OH/O²⁻ species coordinated to Mn³⁺ and Mn²⁺ centers,^{63–66} respectively.

XPS data for the catalytic performance optimization series shown in Figure 1c for the Ni_{0.6}Mn_{0.4}(OH)_y-nS ($1 \leq n \leq 15$) catalysts are given in Figure S3d–f. Ni2p XPS data presented in Figure S3d suggest that increasing the NaOH(aq) concentration in the synthesis protocol from 1S to 9S has a limited influence on Ni2p B.E. However, a further increase in the NaOH(aq) concentration to 12S and 15S results in a Ni2p B.E. shift of –0.3 eV (i.e., from 855.4 to 855.1 eV) that is consistent with the formation of NiO domains,⁶¹ indicating the partial destruction of the bimetallic LDH structure. An analogous behavior is also observed for the Mn2p XPS spectra of these catalysts (Figure S3e) illustrating the formation of shoulder features at 638.4 and 647.6 eV that can be attributed to Mn2p_{3/2} and its satellite signals originating from MnO species.^{63–66} Corresponding O1s XPS spectra (Figure S3f) also exhibit a consistent trend demonstrating the formation of a low B.E. O1s shoulder signal (529.4 eV) at elevated NaOH(aq) concentrations that can be attributed to the partial transformation of hydroxide surface functionalities (531.0 eV) into oxide functionalities. Hence, catalytic activity loss observed in Figure 1c for extremely high NaOH(aq) concentrations can also be linked to the partial transformation of the bimetallic LDH structure into separate NiO and MnO surface domains. Mn AOS values that can be extracted from the corresponding Mn3s XPS spectra for the Ni_{0.6}Mn_{0.4}(OH)_y-nS ($1 \leq n \leq 15$) catalysts (Figure S4) indicate that for the

extremely low NaOH(aq) concentration of 1S, the Mn AOS value is obtained as +3.3, whereas this value increases to +3.4 for the optimum NaOH(aq) concentration of 9S and then reaches +3.6 for an extreme NaOH(aq) concentration of 15S. These results illustrate that an average Mn oxidation state of +3.4 leads to the optimum catalytic performance in the aerobic oxidation of xanthene (**1a**) to xanthone (**1b**) on $\text{Ni}_{0.6}\text{Mn}_{0.4}(\text{OH})_y\text{-}n\text{S}$ (Figure 1c).

3.6. Catalyst Reusability and Regeneration Studies.

In an attempt to test the stability of the optimized catalyst in alkylarene oxidation reactions, catalytic reusability and regeneration experiments were conducted on the optimized $\text{Ni}_{0.6}\text{Mn}_{0.4}(\text{OH})_y\text{-}9\text{S}$ catalyst (Figure S5a,b).

Catalytic reusability experiments were carried out in the oxidation of fluorene (**2a**) by running the catalyst in consecutive catalytic cycles without regeneration. Whereas a high degree of conversion (>99%) to fluorenone (**2b**) was obtained in the first catalytic cycle, the catalytic activity dropped significantly in the second and third consecutive cycles (61 and 19% conversion, respectively, Figure S5a). These results led us to carry out a regeneration protocol to attain high catalytic performance in the subsequent cycles.

Thermal regeneration of the used catalyst in an inert atmosphere can be utilized to eliminate the adsorbates and catalytic poisons that may reside on the catalyst surface after a catalytic run. TGA analysis can be quite informative to avoid any losses in the structural integrity of the catalyst during the thermal regeneration protocol. Weight loss events observed in the TGA experiment presented in Figure S6 can be divided into four stages. In the first stage, a weight loss of 5.2% was detected at 375 K. The second stage led to a 11.4% weight loss at 573 K. The third and fourth stages corresponded 1.7 and 2.1% weight losses at 686 and 897 K, respectively. These four different stages of weight loss can be explained using the former literature studies.¹⁰ The first stage can be attributed to the removal of chemisorbed water from the surface, whereas the second stage can be linked to the desorption of some of the interlayer water molecules. The third stage is associated to the dehydroxylation process, followed by the fourth stage where the metal hydroxide phase is completely dehydroxylated and probably transformed into various oxide phases. With this in mind, we decided to choose 573 K (*i.e.*, a temperature between the second and third weight loss stages in the TGA data) as the regeneration temperature in an attempt to preserve the structural integrity of the material while thermally removing unwanted species from the catalyst surface for the rejuvenation of the material. As shown in the ATR-IR spectroscopic data presented in Figure S7a, although this regeneration procedure leads to some loss in the interlayer water molecules, it does not result in the complete dehydration of the interlayer water, as evidenced by the presence of a broad $-\text{OH}$ vibrational signature within 3000–3500 cm^{-1} after regeneration.

The regeneration protocol was composed of annealing the spent catalyst at 573 K for 6 h (before the second cycle) and for 15 h (before the third cycle) both under 100 sccm 99.999% Ar(g) flow in a tube furnace. Figure S5b clearly shows that the currently utilized regeneration protocol allows complete recovery of the initial catalytic activity after the three consecutive catalytic runs.

To understand the effect of the regeneration protocol on the spent catalyst, ATR-IR spectroscopic studies were conducted on the fresh, spent, and regenerated $\text{Ni}_{0.6}\text{Mn}_{0.4}(\text{OH})_y\text{-}9\text{S}$ catalyst with the aim of investigating the functional group

changes occurring on the catalyst surfaces after reaction and subsequent regeneration steps (Figure S7a).

Assignment of the vibrational features in the ATR-IR spectra given in Figure S7a can be made by using the conventional infrared signatures of common organic functional groups.^{68,69} Spectral features at 1045 and 1100 cm^{-1} can be assigned to $-\text{C}(\text{sp}^3)\text{-O}$ stretching, whereas the IR signals at 1148 and 1230 cm^{-1} can be attributed to $-\text{C}(\text{sp}^2)\text{-O}$ stretching. Carbonate features were also observed at 1449 and 1545 cm^{-1} . On the other hand, the feature seen at 1703 cm^{-1} can be assigned to $-\text{CH}$ or $-\text{CH}_2$ bending modes. Spectral features within 2845–3053 cm^{-1} can be attributed to aliphatic $-\text{CH}_x$ stretching. Figure S7a suggests that after the utilization of the catalyst, various organic residues are deposited on the spent catalyst surface, blocking and poisoning the catalytic active sites. With the help of the control ATR-IR spectroscopic experiments (Figure S8), where we obtained the IR spectra of fluorene, heptane, acetone, and fluorenone and compared them with the IR spectrum of the spent catalyst, it can be realized that the spent catalyst contained adsorbed fluorene (reactant), *n*-heptane (solvent), and fluorenone (product). On the other hand, most of these poisoning species can be eliminated after the regeneration protocol.

In addition to ATR-IR studies, XPS studies were also carried out (Figure S7b–d and Figure S9) to investigate the oxidation state changes occurring on the surface atoms of the $\text{Ni}_{0.6}\text{Mn}_{0.4}(\text{OH})_y\text{-}9\text{S}$ catalyst after the reaction and after undergoing regeneration protocols. Note that XRD analysis of fresh and spent $\text{Ni}_{0.6}\text{Mn}_{0.4}(\text{OH})_y\text{-}9\text{S}$ catalysts (Figure S10) revealed no significant changes in the bulk crystallographic structure of the catalyst. Figure S7d shows that the average Mn oxidation state of the pristine catalyst decreases from +3.4 to +3.1 after each catalytic run (*i.e.*, spent catalyst) and then increases to +3.5 when it is consecutively regenerated. This indicates that with regeneration, the average oxidation state of surface Mn species on the catalyst can be restored to its initial state. Additional XPS data regarding the changes in the Ni2p, O1s, and C1s spectra obtained at various stages of the regeneration experiments can be found in Figure S9. It is likely that the relatively high average oxidation state of Mn cations (*i.e.*, +3.5) and the persistence of the associated $\text{Mn}^{3+/4+}$ species under reaction conditions could be linked to the high reactivity and reusability of the bimetallic $\text{Ni}_{0.6}\text{Mn}_{0.4}(\text{OH})_y\text{-}9\text{S}$ catalyst in the alkylarene and alcohol oxidation. Presumably, $\text{Ni}^{2+/x+}$ cations work in a synergistic manner with Mn sites in the $\text{Ni}_{0.6}\text{Mn}_{0.4}(\text{OH})_y\text{-}9\text{S}$ catalyst structure to stabilize $\text{Mn}^{3+/4+}$ species where the lack of $\text{Ni}^{2+/x+}$ cations leads to a drastic decrease in reactivity due to the reduction of the $\text{Mn}^{3+/4+}$ sites. This is also in accordance with the current catalytic performance data corresponding to the aerobic oxidation of xanthene in Figure 1b for $\text{Mn}(\text{OH})_2$, where the presence of a low nominal Mn oxidation state of +2 and the lack of cooperative $\text{Ni}^{2+/x+}$ cations lead to an extremely limited reactivity, and the former Mn-containing catalysts studied in the literature with reasonable catalytic performances, where the nominal Mn oxidation states were typically high (*e.g.*, >+3, Figure 2 and Table S4).

4. CONCLUSIONS

In summary, a highly effective catalytic method for the benzylic C–H and alcohol oxidation reactions has been developed with the use of $\text{Ni}_{0.6}\text{Mn}_{0.4}(\text{OH})_y\text{-}9\text{S}$, a novel precious metal-free mixed metal hydroxide catalyst with a layered double

hydroxide structure. The catalyst was systematically optimized with respect to the catalyst synthesis method, Ni/Mn metal cation ratio, concentration of NaOH(aq) used for catalyst synthesis, and reaction solvent. The method requires the use of molecular oxygen as the sole stoichiometric oxidant and works successfully with a low catalyst loading on a variety of alkylarenes and alcohols affording oxidation products in excellent yields (93–99%). Compared to the existing catalysts in the literature, the Ni_{0.6}Mn_{0.4}(OH)_y-9S catalyst revealed the best catalytic performance per gram of catalyst in the catalytic aerobic oxidation of xanthene to xanthone. Careful mechanistic studies point to the formation of a radical intermediate during the reaction possibly through a hydrogen atom abstraction mechanism, whereas kinetic isotope effect experiments indicated that the C–H bond activation is the rate-determining step. Finally, a novel catalyst regeneration protocol was developed to fully retain the initial activity of the catalyst after three cycles in the fluorene oxidation reaction. The optimized Ni_{0.6}Mn_{0.4}(OH)_y-9S catalyst was found to reveal (i) rotational faults in its β-Ni_{0.6}Mn_{0.4}(OH)_y domains, (ii) α/β-Ni_{0.6}Mn_{0.4}(OH)_y interstratification disorders, (iii) a relatively high specific surface area of 125 m²/g, (iv) a 2D-platelet morphology with a typical diameter of 50–80 nm, and (v) the presence of Mn³⁺ and Mn⁴⁺ species leading to an average Mn oxidation state of +3.4 operating in a synergistic fashion with the Ni^{2+/x+} cations. Overall, the current results clearly demonstrate that chemically fine-tuned mixed metal hydroxide systems can provide promising catalytic alternatives in low-temperature liquid-phase organic reactions. Further catalytic applications of mixed metal hydroxides are currently under way in our laboratories.

■ ASSOCIATED CONTENT

Supporting Information

The Supporting Information is available free of charge at <https://pubs.acs.org/doi/10.1021/acsanm.2c04634>.

XPS, XRD, BET, TGA, and ATR-IR data for the characterization of catalysts; compilation of literature data for the catalytic performance of heterogeneous aerobic oxidation of xanthene; experimental procedures; and NMR spectra for all organic products (PDF)

■ AUTHOR INFORMATION

Corresponding Authors

Yunus Emre Türkmen – Department of Chemistry, Faculty of Science and UNAM-National Nanotechnology Research Center and Institute of Materials Science and Nanotechnology, Bilkent University, 06800 Ankara, Turkey; orcid.org/0000-0002-9797-2820; Email: yeturkmen@bilkent.edu.tr

Emrah Ozensoy – Department of Chemistry, Faculty of Science and UNAM-National Nanotechnology Research Center and Institute of Materials Science and Nanotechnology, Bilkent University, 06800 Ankara, Turkey; orcid.org/0000-0003-4352-3824; Email: ozensoy@fen.bilkent.edu.tr

Authors

Abel Tetteh Sika-Nartey – Department of Chemistry, Faculty of Science, Bilkent University, 06800 Ankara, Turkey

Yesim Sahin – Department of Chemistry, Faculty of Science, Bilkent University, 06800 Ankara, Turkey; orcid.org/0000-0001-9717-9729

Kerem Emre Ercan – Department of Chemistry, Faculty of Science, Bilkent University, 06800 Ankara, Turkey; orcid.org/0000-0003-4650-7977

Zeynep Kap – Department of Chemistry, Faculty of Science, Bilkent University, 06800 Ankara, Turkey

Yusuf Kocak – Department of Chemistry, Faculty of Science, Bilkent University, 06800 Ankara, Turkey; orcid.org/0000-0003-4511-1321

Ayşe Dilay Erdali – Department of Chemistry, Faculty of Science, Bilkent University, 06800 Ankara, Turkey

Bezanur Erdivan – Department of Chemistry, Faculty of Science, Bilkent University, 06800 Ankara, Turkey; orcid.org/0000-0002-1725-1127

Complete contact information is available at: <https://pubs.acs.org/doi/10.1021/acsanm.2c04634>

Author Contributions

[†]A.T.S.-N. and Y.S. contributed equally to this work.

Notes

The authors declare no competing financial interest.

■ ACKNOWLEDGMENTS

Y.E.T. acknowledges the BAGEP Award of the Science Academy, Turkey.

■ REFERENCES

- (1) Rogge, T.; Kaplaneris, N.; Chatani, N.; Kim, J.; Chang, S.; Punji, B.; Schafer, L. L.; Musaev, D. G.; Wencel-Delord, J.; Roberts, C. A.; Sarpong, R.; Wilson, Z. E.; Brimble, M. A.; Johansson, M. J.; Ackermann, L. C–H Activation. *Nat. Rev. Methods Primers* **2021**, *1*, 43.
- (2) Rej, S.; Das, A.; Chatani, N. Strategic Evolution in Transition Metal-Catalyzed Directed C–H Bond Activation and Future Directions. *Coord. Chem. Rev.* **2021**, *431*, 213683.
- (3) Gandeepan, P.; Müller, T.; Zell, D.; Cera, G.; Warratz, S.; Ackermann, L. 3d Transition Metals for C–H Activation. *Chem. Rev.* **2019**, *119*, 2192–2452.
- (4) Chu, J. C. K.; Rovis, T. Complementary Strategies for Directed C(sp³)–H Functionalization: A Comparison of Transition-Metal-Catalyzed Activation, Hydrogen Atom Transfer, and Carbene/Nitrene Transfer. *Angew. Chem., Int. Ed.* **2018**, *57*, 62–101.
- (5) Sauermann, N.; Meyer, T. H.; Qiu, Y.; Ackermann, L. Electrocatalytic C–H Activation. *ACS Catal.* **2018**, *8*, 7086–7103.
- (6) He, J.; Wasa, M.; Chan, K. S. L.; Shao, Q.; Yu, J.-Q. Palladium-Catalyzed Transformations of Alkyl C–H Bonds. *Chem. Rev.* **2017**, *117*, 8754–8786.
- (7) Santoro, S.; Kozhushkov, S. I.; Ackermann, L.; Vaccaro, L. Heterogeneous catalytic approaches in C–H activation reactions. *Green Chem.* **2016**, *18*, 3471–3493.
- (8) Corey, E. J. Retrosynthetic Thinking—Essentials and Examples. *Chem. Soc. Rev.* **1988**, *17*, 111–133.
- (9) Börgel, J.; Ritter, T. Late-Stage Functionalization. *Chem* **2020**, *6*, 1877–1887.
- (10) Cernak, T.; Dykstra, K. D.; Tyagarajan, S.; Vachal, P.; Krska, S. W. The Medicinal Chemist's Toolbox for Late Stage Functionalization of Drug-like Molecules. *Chem. Soc. Rev.* **2016**, *45*, 546–576.
- (11) Wencel-Delord, J.; Glorius, F. C–H bond activation enables the rapid construction and late-stage diversification of functional molecules. *Nat. Chem.* **2013**, *5*, 369–375.
- (12) Fessner, N. D. P450 Monooxygenases Enable Rapid Late-Stage Diversification of Natural Products via C–H Bond Activation. *ChemCatChem* **2019**, *11*, 2226–2242.

- (13) Pereira, M. M.; Dias, L. D.; Calvete, M. J. F. Metalloporphyrins: Bioinspired Oxidation Catalysts. *ACS Catal.* **2018**, *8*, 10784–10808.
- (14) Wang, V. C.-C.; Maji, S.; Chen, P. P.-Y.; Lee, H. K.; Yu, S. S.-F.; Chan, S. I. Alkane Oxidation: Methane Monooxygenases, Related Enzymes, and Their Biomimetics. *Chem. Rev.* **2017**, *117*, 8574–8621.
- (15) White, M. C. Adding Aliphatic C-H Bond Oxidations to Synthesis. *Science* **2012**, *335*, 807–809.
- (16) Newhouse, T.; Baran, P. S. If C-H Bonds Could Talk: Selective C-H Bond Oxidation. *Angew. Chem., Int. Ed.* **2011**, *50*, 3362–3374.
- (17) Kal, S.; Xu, S.; Que, L., Jr. Bio-inspired Nonheme Iron Oxidation Catalysis: Involvement of Oxoiron(V) Oxidants in Cleaving Strong C-H Bonds. *Angew. Chem., Int. Ed.* **2020**, *59*, 7332–7349.
- (18) Nam, W. High-Valent Iron(IV)-Oxo Complexes of Heme and Non-Heme Ligands in Oxygenation Reactions. *Acc. Chem. Res.* **2007**, *40*, 522–531.
- (19) Chen, M. S.; White, M. C. A Predictably Selective Aliphatic C-H Oxidation Reaction for Complex Molecule Synthesis. *Science* **2007**, *318*, 783–787.
- (20) Guo, Z.; Liu, B.; Zhang, Q.; Deng, W.; Wang, Y.; Yang, Y. Recent advances in heterogeneous selective oxidation catalysis for sustainable chemistry. *Chem. Soc. Rev.* **2014**, *43*, 3480–3524.
- (21) Mizuno, N. Ed. *Modern Heterogeneous Oxidation Catalysis*, Wiley-VCH Weinheim, 2009.
- (22) Punniyamurthy, T.; Velusamy, S.; Iqbal, J. Recent Advances in Transition Metal Catalyzed Oxidation of Organic Substrates with Molecular Oxygen. *Chem. Rev.* **2005**, *105*, 2329–2364.
- (23) Beniya, A.; Higashi, S. Towards dense single-atom catalysts for future automotive applications. *Nat. Catal.* **2019**, *2*, 590–602.
- (24) Bertinchamps, F.; Treinen, M.; Blangenois, N.; Mariage, E.; Gaigneaux, E. M. Positive effect of NO_x on the performances of VO_x/TiO₂-based catalysts in the total oxidation abatement of chlorobenzene. *J. Catal.* **2005**, *230*, 493–498.
- (25) Villa, A.; Wang, D.; Dimitratos, N.; Su, D.; Trevisan, V.; Prati, L. Pd on carbon nanotubes for liquid phase alcohol oxidation. *Catal. Today* **2010**, *150*, 8–15.
- (26) Shan, J.; Li, M.; Allard, L. F.; Lee, S.; Flytzani-Stephanopoulos, M. Mild oxidation of methane to methanol or acetic acid on supported isolated rhodium catalysts. *Nature* **2017**, *551*, 605–608.
- (27) Ihm, S.-K.; Jun, Y.-D.; Kim, D.-C.; Jeong, K.-E. Low-temperature deactivation and oxidation state of Pd/γ-Al₂O₃ catalysts for total oxidation of n-hexane. *Catal. Today* **2004**, *93*, 149–154.
- (28) Thevenin, P. O.; Alcalde, A.; Pettersson, L. J.; Järås, S. G.; Fierro, J. L. G. Catalytic combustion of methane over cerium-doped palladium catalysts. *J. Catal.* **2003**, *215*, 78–86.
- (29) Yamaguchi, K.; Mizuno, N. Supported Ruthenium Catalyst for the Heterogeneous Oxidation of Alcohols with Molecular Oxygen. *Angew. Chem., Int. Ed.* **2002**, *41*, 4538–4542.
- (30) Nielsen, I. S.; Taarning, E.; Egeblad, K.; Madsen, R.; Christensen, C. H. Direct aerobic oxidation of primary alcohols to methyl esters catalyzed by a heterogeneous gold catalyst. *Catal. Lett.* **2007**, *116*, 35–40.
- (31) Powell, A. B.; Stahl, S. S. Aerobic Oxidation of Diverse Primary Alcohols to Methyl Esters with a Readily Accessible Heterogeneous Pd/Bi/Te Catalyst. *Org. Lett.* **2013**, *15*, 5072–5075.
- (32) Kumar, N.; Naveen, K.; Bhatia, A.; Muthaiah, S.; Siruguri, V.; Paul, A. K. Solvent and additive-free efficient aerobic oxidation of alcohols by a perovskite oxide-based heterogeneous catalyst. *React. Chem. Eng.* **2020**, *5*, 1264–1271.
- (33) Zhang, B.-Z.; White, M. A.; Sham, T.-K.; Pincock, J. A.; Doucet, R. J.; Rao, K. V. R.; Robertson, K. N.; Cameron, T. S. Zeolite-Confined Nano-RuO₂: A Green, Selective, and Efficient Catalyst for Aerobic Alcohol Oxidation. *J. Am. Chem. Soc.* **2003**, *125*, 2195–2199.
- (34) Sahin, Y.; Sika-Nartey, A. T.; Ercan, K. E.; Kocak, Y.; Senol, S.; Ozensoy, E.; Türkmen, Y. E. Precious Metal-Free LaMnO₃ Perovskite Catalyst with an Optimized Nanostructure for Aerobic C–H Bond Activation Reactions: Alkylarene Oxidation and Naphthol Dimerization. *ACS Appl. Mater. Interfaces* **2021**, *13*, S099–S110.
- (35) Kawasaki, S.; Kamata, K.; Hara, M. Dioxygen Activation by a Hexagonal SrMnO₃ Perovskite Catalyst for Aerobic Liquid-Phase Oxidation. *ChemCatChem* **2016**, *8*, 3247–3253.
- (36) Sugahara, K.; Kamata, K.; Muratsugu, S.; Hara, M. Amino Acid-Aided Synthesis of a Hexagonal SrMnO₃ Nanoperovskite Catalyst for Aerobic Oxidation. *ACS Omega* **2017**, *2*, 1608–1616.
- (37) Shibata, S.; Sugahara, K.; Kamata, K.; Hara, M. Liquid-phase oxidation of alkanes with molecular oxygen catalyzed by high valent iron-based perovskite. *Chem. Commun.* **2018**, *54*, 6772–6775.
- (38) Hayashi, E.; Tamura, T.; Aihara, T.; Kamata, K.; Hara, M. Base-Assisted Aerobic C-H Oxidation of Alkylarenes with a Murdochite-Type Oxide Mg₆MnO₈ Nanoparticle Catalyst. *ACS Appl. Mater. Interfaces* **2022**, *14*, 6528–6537.
- (39) He, S.; An, Z.; Wei, M.; Evans, D. G.; Duan, X. Layered double hydroxide-based catalysts: nanostructure design and catalytic performance. *Chem. Commun.* **2013**, *49*, 5912–5920.
- (40) Hall, D. S.; Lockwood, D. J.; Bock, C.; MacDougall, B. R. Nickel hydroxides and related materials: a review of their structures, synthesis, and properties. *Proc. R. Soc. A* **2015**, *471*, 20140792.
- (41) Yan, Z.; Yu, X.; Zhang, Y.; Jia, H.; Sun, Z.; Du, P. Enhanced visible light-driven hydrogen production from water by a noble-metal-free system containing organic dye-sensitized titanium dioxide loaded with nickel hydroxide as the cocatalyst. *Appl. Catal. B* **2014**, *160–161*, 173–178.
- (42) Ran, J.; Yu, J.; Jaroniec, M. Ni(OH)₂ modified CdS nanorods for highly efficient visible-light-driven photocatalytic H₂ generation. *Green Chem.* **2011**, *13*, 2708–2713.
- (43) Gao, M.; Sheng, W.; Zhuang, Z.; Fang, Q.; Gu, S.; Jiang, J.; Yan, Y. Efficient Water Oxidation Using Nanostructured α-Nickel-Hydroxide as an Electrocatalyst. *J. Am. Chem. Soc.* **2014**, *136*, 7077–7084.
- (44) Yoshii, D.; Yatabe, T.; Yabe, T.; Yamaguchi, K. C(sp³)-H Selective Benzylic Borylation by In Situ Reduced Ultrasmall Ni Species on CeO₂. *ACS Catal.* **2021**, *11*, 2150–2155.
- (45) Merck KGaA, *Sodium Hydroxide: Properties*. Retrieved on March 12, 2022 from <https://www.sigmaaldrich.com/CA/en/product/sigald/s5881>
- (46) Ogawa, A.; Curran, D. P. Benzotrifluoride: A Useful Alternative Solvent for Organic Reactions Currently Conducted in Dichloromethane and Related Solvents. *J. Org. Chem.* **1997**, *62*, 450–451.
- (47) Potts, D. S.; Bregante, D. T.; Adams, J. S.; Torres, C.; Flaherty, D. W. Influence of solvent structure and hydrogen bonding on catalysis at solid–liquid interfaces. *Chem. Soc. Rev.* **2021**, *50*, 12308–12337.
- (48) Kamlet, M. J.; Abboud, J.-L. M.; Abraham, M. H.; Taft, R. W. Linear Solvation Energy Relationships. 23. A Comprehensive Collection of the Solvatochromic Parameters, π*, α, and β, and Some Methods for Simplifying the Generalized Solvatochromic Equation. *J. Org. Chem.* **1983**, *48*, 2877–2887.
- (49) Kamlet, M. J.; Abraham, M. H.; Doherty, R. M.; Taft, R. W. Solubility Properties in Polymers and Biological Media. 4. Correlation of Octanol/Water Partition Coefficients with Solvatochromic Parameters. *J. Am. Chem. Soc.* **1984**, *106*, 464–466.
- (50) Wang, A.; Zhou, W.; Sun, Z.; Zhang, Z.; Zhang, Z.; He, M.; Chen, Q. Mn(III) active site in hydrotalcite efficiently catalyzes the oxidation of alkylarenes with molecular oxygen. *Mol. Catal.* **2021**, *499*, 111276.
- (51) Buntin, K.; Rachid, S.; Scharfe, M.; Blöcker, H.; Weissman, K.; Müller, R. Production of the Antifungal Isochromanone Ajudazols A and B in *Chondromyces crocatus* Cm c5: Biosynthetic Machinery and Cytochrome P450 Modifications. *Angew. Chem., Int. Ed.* **2008**, *47*, 4595–4599.
- (52) Simmons, E. M.; Hartwig, J. F. On the Interpretation of Deuterium Kinetic Isotope Effects in C-H Bond Functionalizations by Transition-Metal Complexes. *Angew. Chem., Int. Ed.* **2012**, *51*, 3066–3072.
- (53) Goetz, M. K.; Anderson, J. S. Experimental evidence for pKa-driven asynchronicity in C–H activation by a terminal Co(III)-oxo complex. *J. Am. Chem. Soc.* **2019**, *141*, 4051–4062.

(54) Hupe, D. J.; Pohl, E. R. On the magnitude of primary isotope effects for proton abstraction from carbon. *J. Am. Chem. Soc.* **1984**, *106*, 5634–5640.

(55) Hall, S. D.; Lockwood, D. J.; Poirier, S.; Bock, C.; MacDougall, B. R. Raman and Infrared Spectroscopy of α and β Phases of Thin Nickel Hydroxide Films Electrochemically Formed on Nickel. *J. Phys. Chem. A* **2012**, *116*, 6771–6784.

(56) Julien, C. M.; Massot, M.; Poinssignon, C. Lattice vibrations of manganese oxides: Part I. Periodic structures. *Spectrochim. Acta A Mol. Biomol. Spectrosc.* **2004**, *60*, 689–700.

(57) An, Z.; Zhang, W.; Shi, H.; He, J. An Effective Heterogeneous L-Proline Catalyst for the Asymmetric Aldol Reaction Using Anionic Clays as Intercalated Support. *J. Catal.* **2006**, *241*, 319–327.

(58) Shi, H.; He, J. Orientated Intercalation of Tartrate as Chiral Ligand to Impact Asymmetric Catalysis. *J. Catal.* **2011**, *279*, 155–162.

(59) Sommer, R. D.; Rheingold, A. L.; Goshe, A. J.; Bosnich, B. Supramolecular Chemistry: Molecular Recognition and Self-Assembly Using Rigid Spacer-Chelators Bearing Cofacial Terpyridyl Palladium-(II) Complexes Separated by 7 Å. *J. Am. Chem. Soc.* **2001**, *123*, 3940–3952.

(60) Sordyl, J.; Puzio, B.; Manecki, M.; Borkiewicz, O.; Topolska, J.; Zelek-Pogudz, S. Structural Assessment of Fluorine, Chlorine, Bromine, Iodine, and Hydroxide Substitutions in Lead Arsenate Apatites (Mimetites)– $\text{Pb}_5(\text{AsO}_4)_3\text{X}$. *Minerals* **2020**, *10*, 494.

(61) Biesinger, M. C.; Payne, B. P.; Lau, L. W. M.; Gerson, A.; Smart, R. S. C. X-ray photoelectron spectroscopic chemical state quantification of mixed nickel metal, oxide and hydroxide systems. *Surf. Interface Anal.* **2009**, *41*, 324–332.

(62) Wei, S.; Miao, Y. Mn-doped $\text{Ni}(\text{OH})_2$ nanostructures as an efficient electrocatalyst for methanol oxidation in basic solution. *J. Electrochem. Soc.* **2020**, *167*, 104501.

(63) Ubeda, M. H.; Mishima, H. T.; López de Mishima, B. A. The electrochemical response of manganese hydroxide—oxide films in slightly alkaline solutions—I. The redox couple. *Electrochim. Acta* **1991**, *36*, 1013–1018.

(64) Fujiwara, M.; Matsushita, T.; Ikeda, S. Evaluation of Mn 3s X-ray photoelectron spectroscopy for characterization of manganese complexes. *J. Electron Spectrosc. Relat. Phenom.* **1995**, *74*, 201–206.

(65) Gorlin, Y.; Jaramillo, T. F. Investigation of Surface Oxidation Processes on Manganese Oxide Electrocatalysts Using Electrochemical Methods and Ex Situ X-ray Photoelectron Spectroscopy. *J. Electrochem. Soc.* **2012**, *159*, H782–H786.

(66) Di Castro, V.; Polzonetti, G. XPS study of MnO oxidation. *J. Electron Spectrosc. Relat. Phenom.* **1989**, *48*, 117–123.

(67) Galakhov, V. R.; Demeter, M.; Bartkowski, S.; Neumann, M.; Ovechkina, N. A.; Kurmaev, E.; Lobachevskaya, N. I.; Mukovskii, Y. M.; Mitchell, J.; Ederer, D. L. Mn 3s Exchange Splitting in Mixed-Valence Manganites. *Phys. Rev. B* **2002**, *65*, 113102.

(68) Klingenberg, B.; Vannice, M. A. Influence of Pretreatment on Lanthanum Nitrate, Carbonate, and Oxide Powders. *Chem. Mater.* **1996**, *8*, 2755–2768.

(69) Levan, T.; Che, M.; Tatibouet, J. M.; Kermarec, M. Infrared Study of the Formation and Stability of $\text{La}_2\text{O}_2\text{CO}_3$ During the Oxidative Coupling of Methane on La_2O_3 . *J. Catal.* **1993**, *142*, 18–26.

Recommended by ACS

Amorphous Nickel Oxides Supported on Carbon Nanosheets as High-Performance Catalysts for Electrochemical Synthesis of Hydrogen Peroxide

Zekun Wu, Cuijuan Zhang, *et al.*

MAY 04, 2022
ACS CATALYSIS

READ 

Multiple Interface $\text{Ni}(\text{PO}_3)_2\text{-CoP}_4/\text{CoMoO}_4$ Nanorods for Highly Efficient Hydrogen Evolution in Alkaline Water/Seawater Electrolysis

Mei Yang, Huaming Yang, *et al.*

SEPTEMBER 02, 2022
ACS SUSTAINABLE CHEMISTRY & ENGINEERING

READ 

Ultrathin Two-Dimensional Bimetal–Organic Framework Nanosheets as High-Performance Electrocatalysts for Benzyl Alcohol Oxidation

Yujing Song, Wenkai Zhang, *et al.*

MAY 04, 2022
INORGANIC CHEMISTRY

READ 

Reconstruction of Ni–Co Phosphites Precatalyst into Metal Oxyhydroxides for Durable Full Water Electrolyzer Cell

S. Chandra Sekhar, Jae Su Yu, *et al.*

OCTOBER 20, 2022
ACS SUSTAINABLE CHEMISTRY & ENGINEERING

READ 

Get More Suggestions >